Monthly Notices of the ROYAL ASTRONOMICAL SOCIETY

MNRAS **529,** 4176–4191 (2024) https://doi.org/10.1093/mnras/stae672
Advance Access publication 2024 March 06

Asteroseismic modelling of the chemically peculiar B-type pulsator with an asymptotic period spacing – a Cen

Przemysław Walczak ★ and Agnieszka Kopacz
University of Wrocław, Faculty of Physics and Astronomy, pl. Uniwersytecki 1, PL-50-137 Wrocław, Poland

Accepted 2024 March 1. Received 2024 March 1; in original form 2023 May 23

ABSTRACT

A Cen is recognized as a magnetic variable star with peculiar helium abundance. The presence of large surface spots induces flux modulation, allowing for the derivation of the surface rotational period (∼8.8 d). *TESS* photometry has unveiled additional signals that we interpreted as SPB-type pulsation. Furthermore, we managed to find a regular period spacing pattern and hence identified pulsational modes. We performed an asteroseismic analysis that resulted in constraints for internal structure of the star. Taking into account the surface rotation period derived from spots and the internal rotation obtained from asteroseismology, we concluded that the gradient of the rotational velocity in the radial direction is very small, indicating nearly solid body rotation. We also constrained overshooting from the convective core, as well as the mass and metallicity of the star.

Key words: stars: abundances – stars: individual: a Cen – stars: oscillations – stars: rotation.

1 INTRODUCTION

Asteroseismology based on space observations allows us to probe stellar interiors with unprecedented precision (e.g. Bowman 2020; Aerts 2021). The observed oscillations can be used as a scanner that probes different stellar layers (Unno et al. 1989; Aerts, Christensen-Dalsgaard & Kurtz 2010). This includes studying the transport of angular momentum and mixing processes of chemical elements (e.g. Aerts et al. 2018; Aerts, Mathis & Rogers 2019; Pedersen et al. 2021).

In the late B-type stars, the opacity mechanism operating in the *Z*-bump effectively excites high order *g*-modes (e.g. Dziembowski, Moskalik & Pamyatnykh 1993; Gautschy & Saio 1993). In this kind of oscillation, the dominant restoring force is buoyancy, and the stars that pulsate in such modes are called Slowly Pulsating B-type stars (SPB; Waelkens 1991).

The *g*-mode pulsations are sensitive to the deep, near core regions of main sequence stars (Aerts et al. 2018). However, the pulsational modes can be used in analysis only when successful identification is available, i.e. the mode degrees ℓ, azimuthal orders m, and radial orders n are known.

There are a few methods of mode identification. All of them require specific observations. For example, multicolour photometry (Daszyńska-Daszkiewicz, Dziembowski & Pamyatnykh 2003, 2005) or spectroscopy (Zima 2006; Zima et al. 2006). Such requirements are difficult to meet in the case of many stars, which are observed from space. Fortunately, the asymptotic theory of oscillations, that can be applied in the case of high order *g*-modes, predicts a regular period spacing between consecutive radial orders for a given ℓ and m (e.g. Shibahashi 1979; Tassoul 1980; Dziembowski, Moskalik & Pamyatnykh 1993; Bouabid et al. 2013). Therefore, identification of regularities in the oscillation spectrum, in principle, enables mode identification (Aerts 2021).

In the case of the homogeneous and non-rotating stars, pulsational period of mode degree ℓ and radial order n approximately follow the relation

$$P_{n\ell} = \frac{\Pi_0}{\sqrt{\ell(\ell+1)}}, \tag{1}$$

where

$$\Pi_0 = \pi \left(\int \frac{N}{r} \mathrm{d}r \right)^{-1}, \tag{2}$$

N is a square root of the Brünt-Väisalä frequency and ϵ is a small constant that depends on the boundary conditions of the propagation zone.

Pulsational periods can be affected by different effects, causing deviations from a value given by equation (1). For example, the rotation can change the periods quite significantly. Rotation lifts the frequency degeneracy, causing the period to also depend on the azimuthal number, m. Other important factors are inhomogeneities of the chemical element abundances, which cause deviations from the linear relation of period differences. Gradients in the chemical element abundances appear as dips (so called buoyancy glitches) in the period-spacing patterns (Dziembowski, Moskalik & Pamyatnykh 1993; Miglio et al. 2008).

Sequences of quasi-regular period spacings in many B-type stars were found by multiple authors (e.g. Degroote et al. 2010; Pápics et al. 2014; Moravveji et al. 2015; Pápics et al. 2015; Triana et al. 2015; Moravveji et al. 2016; Pápics et al. 2017; Szewczuk, Daszyńska-Daszkiewicz & Walczak 2017; Szewczuk & Daszyńska-Daszkiewicz 2018; Zhang et al. 2018; Pedersen et al. 2021; Szewczuk, Walczak & Daszyńska-Daszkiewicz 2021; Garcia et al. 2022; Niemczura et al. 2022). The data were then very often subjects of detailed studies that resulted in the determination

★ E-mail: przemyslaw.walczak@uwr.edu.pl

Table 1. *TESS* observations of a Cen. The last column provides the number of observations.

Sector	Dates (UTC)	Cycle	Camera	CCD	Cadence	*N*
11	22 Apr–21 May 2019	1	1	2	120 s	11684
38	28 Apr–26 May 2021	3	1	1	120 s	18048
65	4 May–6 June 2023	5	1	1	120 s	17826

of internal rotation velocities (Pedersen et al. 2021; Niemczura et al. 2022) and putting constraints on chemical element transport (Christophe et al. 2018; Takata et al. 2020; Pedersen et al. 2021; Mombarg et al. 2022; Szewczuk et al. 2022).

In overall, the asteroseismic studies suggest that the angular momentum transport is quite effective, leading to the nearly rigid rotation of the main sequence stars. Additionally, asteroseismic models usually require some additional mixing of chemical elements. All of this indicates that some processes that govern stellar structure and evolution are missing or not well calibrated/described. In this work, we analysed one more B-type star, which will add a piece of information to the theory of internal structure and evolution.

In Section 2, we give a short description of a target star, a Cen, and describe its photometric observations analysis. Section 3 contains results of our asteroseismic modelling. Conclusions are summarized in Section 4.

2 A CEN

A Cen (HD 125823) is a chemically peculiar B-type star. Its surface inhomogeneities cause rotational variability with a period of 8.816991(9) days (Krtička et al. 2020). According to Krtička et al. (2020), a Cen exhibits the most extreme variation of He abundance across its surface of any known He-peculiar star. Its apparent magnitude in *V* filter is 4.42 mag (Fossati et al. 2015) and in *Gaia G* filter is 4.36 mag (Gaia Collaboration 2018). The effective temperature, $\log T_{\rm eff} = 4.279(46)$ K, was taken from Bohlender, Rice & Hechler (2010); Krtička et al. (2020); Shultz et al. (2022).

We calculated the luminosity by taking into account the *Gaia* DR3 parallax $\pi = 8.33(18)$ mas (Gaia Collaboration 2023) and bolometric corrections from Pedersen et al. (2020) applied to *V* and *G* filters. We also included the extinction $A_V = 0.21$ and $A_G = 0.20$ that we derived from reddening $E(B-V) = 0.07$ (Gontcharov & Mosenkov 2017) and the total to selective absorption coefficients $R_V = 3.089$ and $R_G = 3.002$ (Fitzpatrick 2004). The final luminosity cover results from both filters are $\log L/L_\odot = 3.10(12)$.

The measurements of the rotational velocity in the direction towards the observer are ambiguous and range from 15 to 30 km s^{-1} (Głębocki & Gnaciński 2005).

The star pulsates also in high-order *g*-modes, indicating, that a Cen is an SPB type star (Sharma et al. 2022). We performed a detailed analysis of the variability of the star using data collected by the *TESS* satellite (Ricker et al. 2015; Ricker 2019). The object was observed in three sectors, 11, 38, and 65. The detailed information on the observations are given in Table 1.

The 2-min TESS cadence light curves and FFI images were downloaded from the Mikulski Archive for Space Telescopes[1] (MAST). Initially, we analysed both types of the available 2-min cadence data, Simple Aperture Photometry (SAP) fluxes and the

[1] https://archive.stsci.edu/

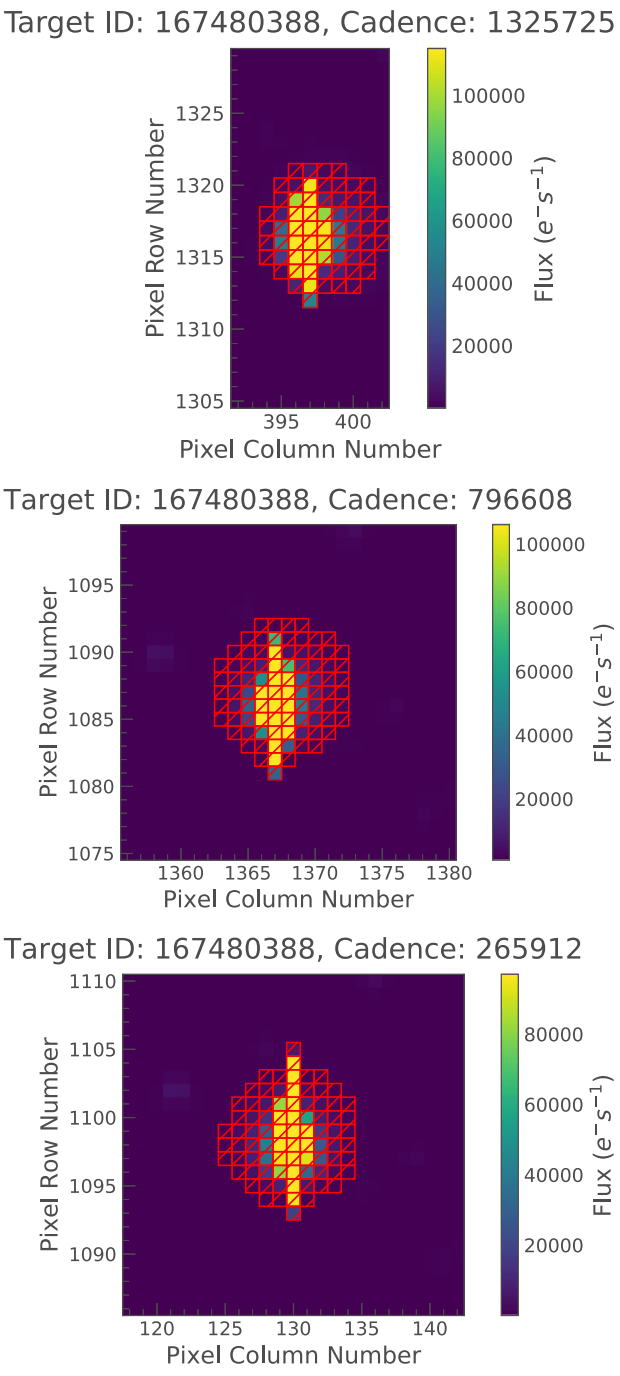

Figure 1. The star images captured by the *TESS* satellite in sector 65 (upper panel), 38 (middle panel), and 11 (bottom panel). The photometric aperture, highlighted with red squares, was manually selected. Image comes from the PYTHON LIGHTKURVE package.

Pre-search Data Conditioning SAP (PDCSAP) fluxes, the latter corrected for instrumental effects (Jenkins et al. 2016). In the end, however, we decided to apply our own apertures, shown in Fig. 1. The default aperture is smaller and does not cover all pixels with a signal. Applying our apertures resulted in a smaller noise level in very low frequencies and we used them in our further analysis.

We utilized the LIGHTKURVE package (https://docs.lightkurve.org/, Lightkurve Collaboration 2018) as well as ASTROPY (Astropy Col-

laboration 2022) and ASTROQUERY packages (Ginsburg et al. 2019) to extract light curves from selected apertures. The data from sector 11 was less numerous, and there is a gap in the observations, leading to significant aliases visible in the frequency spectrum. Therefore, the analysis of sector 11 had to be performed with special caution.

2.1 Fourier analysis

The light curves from all sectors underwent a thorough analysis, encompassing the computation of the Fourier frequency spectrum, identification of the highest maximum in the spectrum, and pre-whitening the original light curves from all previously detected frequencies.

We calculated a Lomb–Scargle periodograms (Lomb 1976; Scargle 1982) using an algorithm based on non-equally spaced fast Fourier transforms (e.g. Leroy 2012). Subsequently, a non-linear least square fitting of a function was performed:

$$m(t) = \sum_{i=1}^{n} A_i \sin(2\pi(t - T_0)f_i + \phi), \tag{3}$$

where, $m(t)$ represents the brightness of the star, t denotes time, and f_i, A_i, and ϕ are adjustable parameters corresponding to frequency, amplitude, and phase, respectively. The value of T_0 was selected as the time of the first observation, determined separately for each sector.

For sector 11, we found 13 independent frequencies for sector 38, we derived 22 independent frequencies and for sector 65, we obtained 18 independent frequencies. The search for frequencies ranged from 0 up to 10 d^{-1}. The noise was computed as the average signal across the entire studied frequency range after each pre-whitening process.

As a significance indicator, we took signal-to-noise ratio (S/N) greater than 5. Such a value for *TESS* data was suggested by Baran & Koen (2021), but we performed an independent analysis, that resulted in a similar threshold. We generated 500 000 synthetic light curves, assuming they consist only of Gaussian noise. The points in the light curves were taken at exactly the same time as original light curve therefore our simulation was personalized for *TESS* observation of a Cen. For every light curve, we calculated the Fourier frequency spectrum and took the highest S/N peak. The highest value of S/N occurs at about 5.1, but the 99.9 per cent of the S/N occurrence is below 4.4. Therefore, S/N $>$ 5.0 seems to be a very safe criterion. The noise in the simulation was calculated in the same manner as in the case of the original light curve.

In the upper panel of Fig. 2, the light curve of a Cen obtained by *TESS* in Sector 65 is presented. The middle panel displays the periodogram calculated for this data, while the bottom panel shows a periodogram after removing all significant frequencies. In Figs 3 and 4, we showed the same as in Fig 2, but for Sector 38 and 11, respectively. The list of derived frequencies from all sectors is provided in Table 2.

Statistically significant signals appear only for low frequencies, $\lesssim$4 d^{-1}. The dominant frequency, 0.1133 d^{-1}, is a rotational frequency. We have also found its four harmonics. The highest pulsational frequency is 1.1750 d^{-1}, and it was already derived from *TESS* data by Sharma et al. (2022). The majority of other pulsational modes exhibit frequencies in the range 0.5–2 d^{-1}, characteristic of SPB variables. The frequencies from different sectors generally exhibit good agreement with each other. However, some frequencies are unique to one or two sectors. Additionally, most frequencies

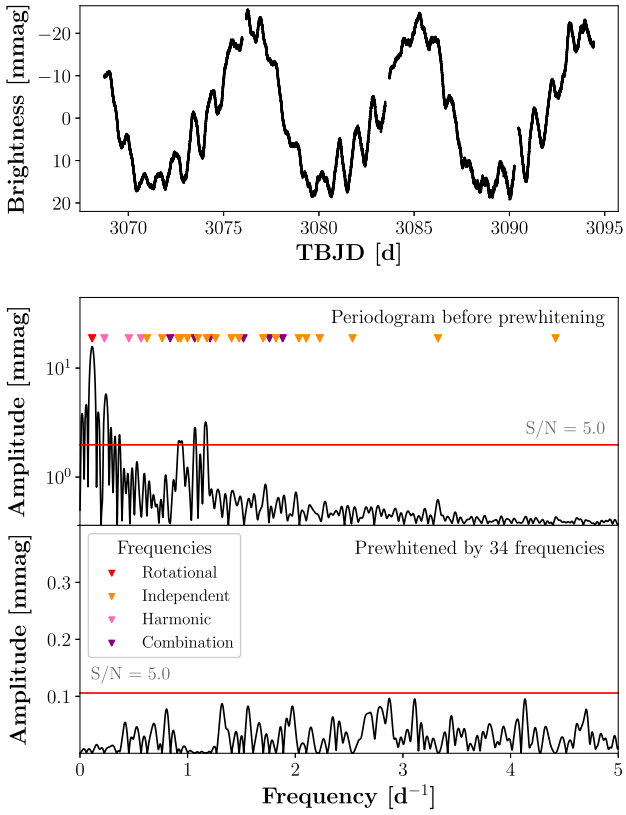

Figure 2. Upper panel: *TESS* light curve from Sector 65. Middle panel: the classical amplitude spectrum of the original data of a Cen. On the horizontal axis is truncated Barycentric Julian date. Bottom panel: periodogram after prewhitening by 31 frequencies. In the middle and bottom panels, we marked a signal-to-noise level of 5.0. Triangles shown in the middle panel indicate detected frequencies.

experience variable amplitudes, and in certain sectors, they may fall below the detection threshold.

In general, the frequencies appear to be well resolved in the periodograms, with a typical half-width of a peak around $\sim$0.04, equivalent to the reciprocal of the time span of observations, ΔT = 26.36 d. The Rayleigh resolution is 0.019 d^{-1}. Therefore, the potential problem with resolution can occur for the f_2 frequency, which is close to the fifth harmonic of f_1 (with a frequency difference $\delta\nu$ = 0.009 d^{-1}). Frequencies near the resolution border include f_5 and f_6 with $\delta\nu$ = 0.015 d^{-1}, f_8 and the combination $f_{17} - 5f_1$ with $\delta\nu$ = 0.017 d^{-1}, f_{14}, and f_{15} with $\delta\nu$ = 0.016 d^{-1}, f_7 and the combination f_{17}–$5f_1$ with $\delta\nu$ = 0.014 d^{-1}.

The nearest bright object, HD 125805, is a K3III type star with visual magnitude V = 6.81 and it is 7 arc minutes away from a Cen. To determine whether contamination plays any role in the TESS data, we downloaded TESS 2-min cadence light curves for this nearest star and performed Fourier analysis. HD 125805 was observed in the same sectors as a Cen. The star is variable with considerable changes of frequencies and amplitudes that are visible from sector to sector. The dominant variability frequencies are of the order of 0.27, 0.61, and 0.13 d^{-1} and have amplitudes $\sim$0.4 mmag. Therefore, it seems that it does not contribute to light variability of a Cen.

The contribution of the other sources is negligible because they are at least several magnitudes fainter than a Cen.

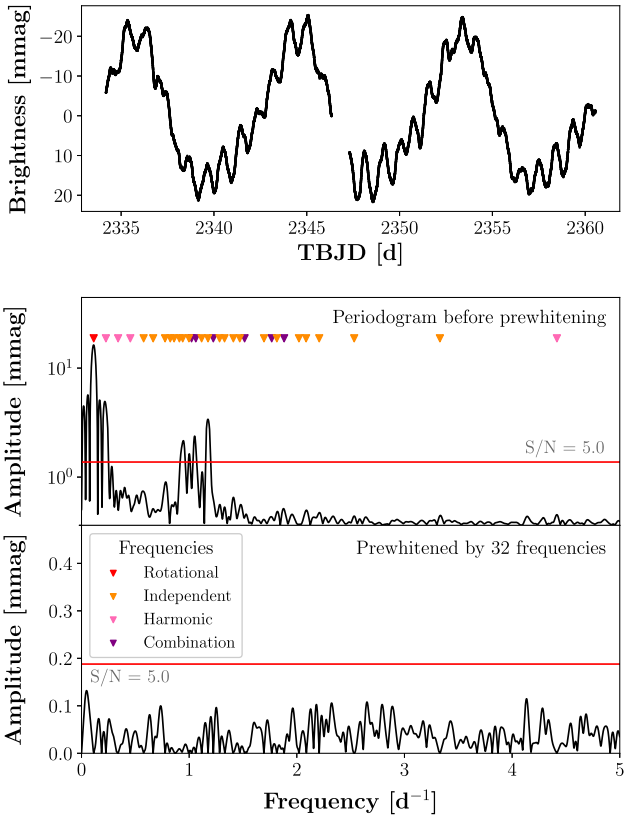

Figure 3. Upper panel: *TESS* light curve from Sector 38. Middle panel: the classical amplitude spectrum of the original data of a Cen. Bottom panel: periodogram after prewhitening by 32 frequencies. In the middle and bottom panels, we marked a signal-to-noise level of 5.0.

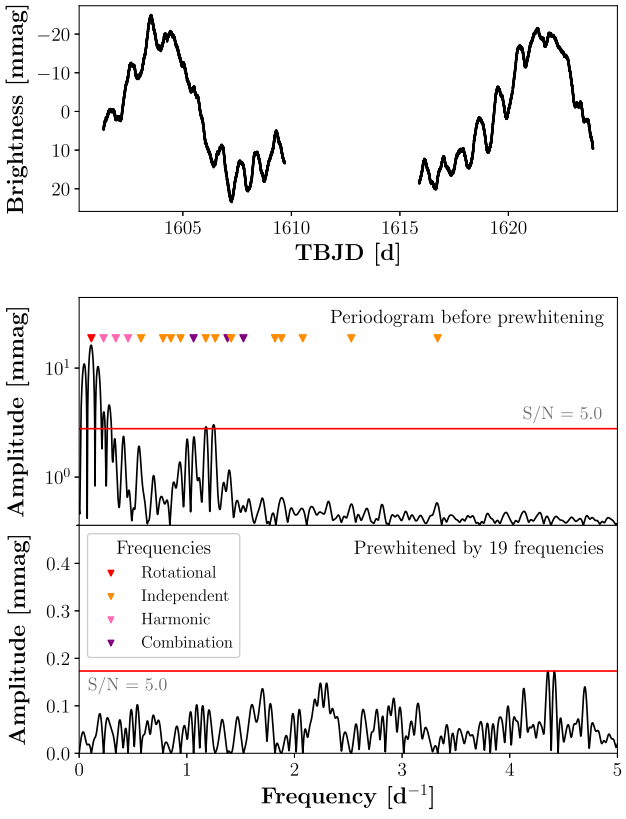

Figure 4. Upper panel: *TESS* light curve from Sector 11. Middle panel: the classical amplitude spectrum of the original data of a Cen. Bottom panel: periodogram after prewhitening by 19 frequencies. In the middle and bottom panels, we marked a signal-to-noise level of 5.0.

2.2 Asymptotic signature

In *TESS* data, we found low frequencies corresponding to the SPB-type pulsations. The analysis of the oscillation spectrum revealed the presence of a quasi regular period spacing feature that we called S_a. It consists of 11 pulsational modes written in Table 3. The period differences versus period is shown in Fig. 5. The sequence ranges from 0.77 d^{-1} up to 2.2 d^{-1}.

We assumed that frequencies from S_a have the same mode degree and azimuthal number and performed an extensive asteroseismic modelling. We concluded that the series S_a is best reproduced by the dipole prograde modes ($\ell = 1$, $m = 1$) of consecutive radial orders. In the last column of Table 3, we provided the radial orders that resulted from our asteroseismic modelling. The details are described in Sect. 3.2.

From Fig. 5, we see that the period differences of the sequence decrease slowly with period. The overall shape of ΔP is quite a smooth function of P. There are glitches near periods 1–1.2 d, indicating inhomogeneities in the chemical element abundances. The sequence S_a was used in subsequent asteroseismic modelling, that brought some constraints on various physical parameters describing internal structure of the star.

3 ASTEROSEISMIC ANALYSIS

Forward asteroseismic modelling depends on fitting the values of the identified observed pulsational frequencies to theoretical counterparts. In the case of a Cen, we made use of additional data that constrain stellar parameters. This includes position of the star in the HR diagram and the surface rotational frequency.

In Fig. 6, we showed the HR diagram with the position of a Cen. The star appears to be a young main sequence object with a mass of approximately 5 $M_\odot$. Further discussion on the marked models is provided later in the text.

3.1 Evolutionary and pulsational codes

All evolutionary models were calculated with the MESA code (see Paxton et al. 2011, 2013, 2015, 2018, 2019, and references therein) ver.15140. We used the MESA equation of state (EOS), which is a blend of the OPAL (Rogers & Nayfonov 2002), SCVH (Saumon, Chabrier & van Horn 1995), PTEH (Pols et al. 1995), HELM (Timmes & Swesty 2000), and PC (Potekhin & Chabrier 2010) EOSes. Nuclear reaction rates were taken from JINA REACLIB (Cyburt et al. 2010) plus additional tabulated weak reaction rates (Fuller, Fowler & Newman 1985; Oda et al. 1994; Langanke & Martínez-Pinedo 2000). Screening was included via the prescriptions of Salpeter (1954), Dewitt, Graboske & Cooper (1973), Alastuey & Jancovici (1978), Itoh et al. (1979), while thermal neutrino loss rates were taken from Itoh et al. (1996). In all computations, we used the solar chemical element mixture from Asplund et al. (2009) and applied the exponentially decaying overshooting from the convective core (Herwig 2000).

The evolution tracks presented in Fig. 6 were calculated with metallicity $Z = 0.010$, initial hydrogen abundance $X_{ini} = 0.70$, and initial rotational velocity on ZAMS (Zero Age Main Sequence) $V_{rot,0}$

Table 2. Results of frequency analysis of *TESS* data of a Cen in sectors 65 (left side), 38 (middle section), and 11 (right side). In the final column, we provide the average frequency, weighted by signal-to-noise ratio.

	Sector 65			Sector 38			Sector 11			Average
No.	Frequency	Amplitude	S/N	Frequency	Amplitude	S/N	Frequency	Amplitude	S/N	Frequency
f_1	0.1134800(46)	17.9409(42)	52.9	0.1133130(62)	17.7974(54)	70.3	0.1134782(56)	17.7120(58)	45.0	0.11341(10)
$2\,f_1$	0.2269600	4.059(42)	26.0	0.2266260	3.9335(57)	28.0	0.2269564	4.0460(61)	19.0	0.22683(20)
$3\,f_1$	0.3404399	0.1736(42)	5.9	0.3399390	0.2886(57)	7.7	0.3404346	0.2537(59)	2.8	0.34020(31)
$4\,f_1$	0.4539198	0.3227(41)	7.4	0.4532520	0.1574(58)	5.2	0.4539128	0.3557(62)	6.4	0.45374(36)
$5\,f_1$	0.5673998	0.6581(42)	9.1	–	–	–	–	–	–	0.567400
f_2	–	–	–	0.57711(44)	0.3124(57)	6.6	0.57490(27)	0.4768(62)	8.3	0.5759(16)
f_3	0.62566(39)	0.2422(43)	7.0	–	–	–	–	–	–	0.62566(39)
f_4	–	–	–	0.66556(49)	0.1934(57)	6.9	–	–	–	0.66556(49)
f_5	0.76248(20)	0.5093(43)	9.0	–	–	–	–	–	–	0.76248(20)
f_6	–	–	–	0.77622(19)	0.9061(58)	13.7	0.77934(23)	0.6758(92)	5.1	0.7771(20)
f_7	–	–	–	0.82435(44)	0.3238(58)	7.2	–	–	–	0.82435(44)
$f_{17} - 5f_1$	0.84105	0.3546(46)	6.6	–	–	–	–	–	–	0.84105
f_8	–	–	–	0.86032(32)	0.2763(43)	5.5	0.85207(22)	0.9749(88)	9.4	0.8551(56)
f_9	0.9032490	0.5415(66)	8.9	0.90897(39)	0.6509(71)	9.1	–	–		0.9061(40)
f_{10}	0.93666(11)	1.6862(66)	17.6	0.94005(14)	1.6568(79)	17.5	0.94196(96)	1.7106(67)	15.7	0.9395(27)
f_{11}	1.0014400(60)	0.9952(48)	12.4	0.99775(10)	1.1420(63)	18.0	–	–	–	0.9993(26)
$f_1 + f_9$	–	–	–	1.02229	0.1998(43)	6.1	–	–	–	1.02229
$f_{13} - f_1$	1.0647474	1.7019(84)	17.0	1.061649	1.7055(60)	20.0	1.063111	1.5662(64)	18.0	1.0631(16)
f_{12}	1.10931(46)	0.7706(71)	8.5	1.11575(33)	0.2679(43)	5.9	–	–	–	1.1119(45)
$f_{14} - f_1$	1.15483	0.516(13)	5.4	–	–	–	–	–	–	1.15483
f_{13}	1.178227(25)	2.1884(14)	25.7	1.174962(41)	2.5849(59)	26.1	1.176589(53)	2.5006(72)	20.3	1.1766(17)
$2\,f_1 + f_{11}$	1.22840	0.3986(69)	8.6	1.22437	0.6703(61)	10.0	–	–	–	1.2262(28)
f_{14}	1.26831(30)	0.5378(45)	9.0	–	–	–	1.26444(18)	0.9199(61)	11.1	1.2662(27)
f_{15}	–	–	–	1.28240(75)	0.3261(68)	7.6	–	–	–	1.28240(75)
f_{16}	–	–	–	1.32853(64)	0.2796(67)	6.1	–	–	–	1.32853(64)
$f_1 + f_{14}$	–	–	–	–	–	–	1.37791	0.2777(69)	5.3	1.37791
f_{17}	1.40845(17)	0.5568(43)	8.5	1.41053(21)	0.6096(65)	9.7	1.41244(27)	0.5322(61)	7.9	1.4104(19)
f_{18}	1.478334(57)	0.4283(44)	8.6	1.46981(27)	0.4708(59)	8.4	–	–	–	1.4741(60)
$3\,f_1 + f_{13}$	1.51867	0.2169(45)	6.2	1.514901	0.1621(43)	5.6	1.52592	0.4470(60)	7.9	1.5205(57)
$3f_1 + f_{14}$	1.60875	0.1412(43)	5.6	–	–	–	–	–	–	1.60875
f_{19}	1.70277(26)	0.3789(43)	7.4	1.69533(61)	0.1510(43)	5.1	–	–	–	1.6997(52)
$2\,f_{10} - f_1$	1.75983	0.1703(43)	5.3	1.76678	0.1578(43)	5.3	–	–	–	1.7633(49)
f_{20}	1.8209820(70)	0.3372(44)	7.1	1.81454(37)	0.3385(57)	7.2	1.81972(43)	0.3018(75)	7.6	1.8184(34)
$2\,f_{11} - f_1$	1.88940	0.2410(43)	7.0	1.88218	0.3645(57)	6.5	1.87943(35)	0.3556(75)	5.4	1.8841(52)
f_{21}	2.03173(17)	0.1512(42)	5.3	2.01977(50)	0.1861(45)	5.4	–	–	–	2.0257(85)
f_{22}	–	–	–	2.08627(40)	0.3136(56)	6.8	2.07735(41)	0.3102(61)	6.2	2.0820(63)
f_{23}	2.2030(13)	0.3160(37)	5.4	2.20811(24)	0.3000(55)	6.9	–	–	–	2.2059(36)
f_{24}	2.2982(13)	0.0763(43)	5.6	–	–	–	–	–	–	2.2982(13)
f_{25}	2.53250(41)	0.2136(41)	6.1	2.53298(63)	0.1728(55)	5.4	2.52807(64)	0.1922(59)	5.3	2.5313(27)
f_{26}	3.32514(27)	0.3268(41)	7.6	3.32934(45)	0.2554(55)	6.7	3.33012(41)	0.2989(59)	6.6	3.3281(27)
f_{27}	4.27531(78)	0.1127(41)	5.1	–	–	–	–	–	–	4.27531(78)
$2\,f_{23}$	–	–	–	4.41621	0.1822(55)	5.4	–	–	–	4.41621

Table 3. List of frequencies comprising the S_a sequence. The subsequent columns include frequency number (ID), frequency (f), period (P), period difference (ΔP), amplitude (A), and radial order.

No	f (d^{-1})	P (d)	ΔP (d)	A (mmag)	
f_6	0.7771	1.2869	0.0738	0.9061	g_{14}
f_7	0.82435	1.2131	0.0436	0.3238	g_{13}
f_8	0.8551	1.1694	0.1050	0.2763	g_{12}
f_{10}	0.9395	1.0644	0.0634	1.6568	g_{11}
f_{11}	0.9993	1.0011	0.0605	1.142	g_{10}
$f_{13} - f_1$	1.0631	0.94058	0.0907	1.7055	g_9
f_{13}	1.1766	0.84992	0.0972	2.5849	g_8
f_{16}	1.32853	0.75271	0.0934	0.2796	g_7
$3f_1 + f_{13}$	1.5205	0.65928	0.1094	0.1621	g_6
f_{20}	1.8184	0.54993	0.1148	0.3385	g_5
f_{23}	2.2059	0.43510	–	0.3160	g_4

$= 20\,\mathrm{km\,s^{-1}}$. We also used the OPLIB opacity tables (Colgan et al. 2015, 2016) supplemented with the data provided by Ferguson et al. (2005) for low-temperature region.

The adiabatic and non-adiabatic pulsational models were calculated with our own code, which solves the linearized stellar pulsation equations (e.g. Unno et al. 1989). Since our main interest is high-order g-modes, we applied the traditional approximation to include the effects of rotation (Chapman & Lindzen 1970; Unno et al. 1989; Bildsten, Ushomirsky & Cutler 1996; Lee & Saio 1997; Townsend 2003a, b; Daszynska-Daszkiewicz, Dziembowski & Pamyatnykh 2007; Dziembowski, Daszyńska-Daszkiewicz & Pamyatnykh 2007). Pulsational equations are given in Appendix B. This approach is suitable for the slow-to-moderate rotation (e.g. Ballot, Lignières & Reese 2013).

In the code, a care has been taken to appropriately increase the mesh density whenever it is needed. The asymptotic expressions

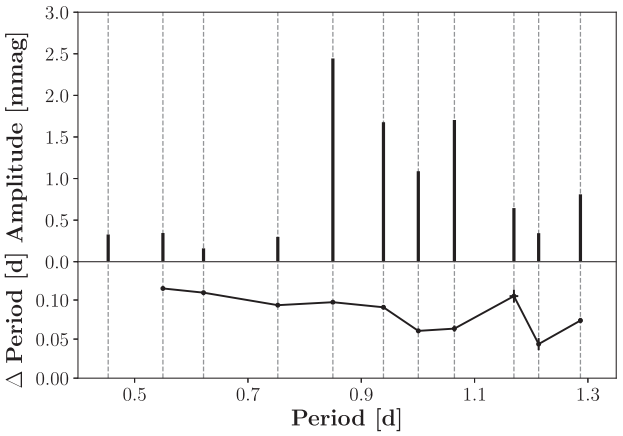

Figure 5. Quasi-regular period spacings found in the oscillation spectrum of a Cen. The upper panel displays the periods and amplitudes of detected modes from S_a. The bottom panel presents the period differences. The errors are typically smaller than the symbols.

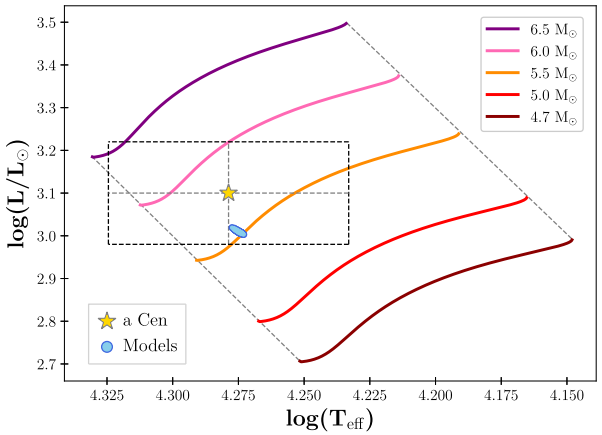

Figure 6. The HR diagram with the position of a Cen along with five evolutionary tracks corresponding to different masses (indicated in the legend) and initial parameters: $Z = 0.01$, $Y = 0,029$, $f_{ov} = 0.01$, $V_{rot,0} = 30\,\mathrm{km\,s^{-1}}$. The blue dotes represent our asteroseismic models calculated with the OPLIB opacities, initial hydrogen abundance $X_{ini} = 0.7$, and rotational mixing processes (details are given in the text). The left and right dotted lines correspond to the zero age main sequence and terminal age main sequence, respectively.

for wavelength were used to estimate the maximal difference in the radius between consecutive layers (see, for example, Chapter 15 in Unno et al. 1989). This criterion ensures that at least a few mesh points fall within a wavelength. Similar approach was applied in the Dziembowski code (Dziembowski 1977). In the pressure mode cavity, we used expression for p-modes, and in the gravity mode cavity, we used formula for g-modes. The wavelength is frequency dependent and in the case of high order modes it can lead to a large mesh density. This, obviously, slows down the calculations, but ensures the correct results of numerical calculations.

The radial differential rotation was also taken into account. The rotational velocity profiles were provided by the MESA code, which treats the angular momentum transport in a diffusion approximation (Endal & Sofia 1978; Pinsonneault et al. 1989; Heger, Langer & Woosley 2000).

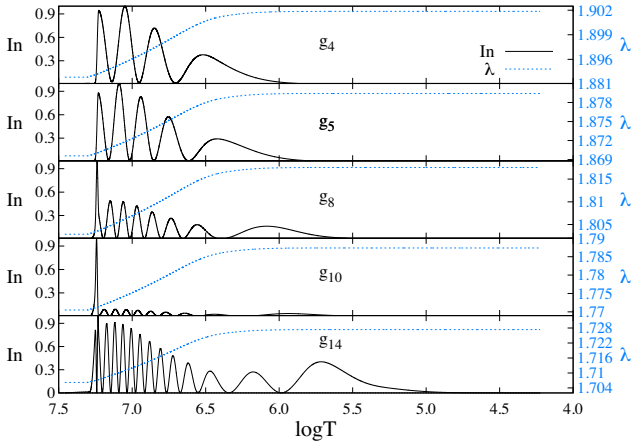

Figure 7. Left-hand axis: mode inertia, In, with arbitrary normalization, as a function of temperature for five selected dipole prograde modes. Right-hand axis: eigenvalue of the Laplace tidal equation, λ, for a given mode.

We calculated a large grid of evolutionary and pulsational models. We search metallicity from 0.006 to 0.025, rotational velocity from 0 to 50 km s^{-1}, mass from 4.0 to 6.0 $M_\odot$, and overshooting parameter from 0.0 up to 0.4. We assumed initial hydrogen abundance, $X = 0.7$ and tested three different opacity tables OPAL (Iglesias & Rogers 1996), OP (Seaton 2005), and OPLIB (Colgan et al. 2015, 2016). Our grids consist of mostly adiabatic pulsational models. Non-adiabatic calculations are much more time (and computer resources) consuming. Therefore, non-adiabatic calculations were performed only in the case of the most interesting situations (see Sect. 3.3).

Comparison of the observed sequence of frequencies, S_a, with theoretical ones showed that the series can be reproduced only by prograde dipole modes. Therefore, we had in our disposal well-identified modes that could be used in a detailed forward asteroseismic modelling. Additionally, we used other very important observational constraint, namely surface rotational frequency. This frequency was determined with high precision and, for a given radius, it sets the value of the surface rotational velocity.

In principle, the determination of the radial orders of frequencies from sequences like S_a are ambiguous. Fortunately, in our case, it was possible to derive the radial orders precisely. To do this, we used an accurate determination of the effective temperature and luminosity of the star. The sequence contains modes with radial order from $n = -14$ to -4. Other ranges of n produce models that lay far outside the error box in the HR diagram.

The sequence S_a consists of modes with different propagation zones. The inertia for five chosen modes of an exemplary model are shown in Fig. 7. The g_4 mode depends mostly on the physical properties of layers between $\log T \sim 6.0$ to 7.2. Higher radial order modes are consecutively more sensitive to the shallower layers. The g_{14} mode depends on the layers up to $\log T \sim 5.2$. Therefore, by means of asteroseismic analysis, we were able to scan a quite significant part of the star. In the figure, we observe an intriguing behaviour of the g_{10} mode. This mode was effectively trapped in the proximity of the high gradient of the chemical abundance near the convective core. As a result, its properties are highly sensitive to that specific region.

On the right-hand axis of Fig. 7, we plotted the eigenvalue of the Laplace tidal equations, λ, a component of the traditional approximation of rotation (see Appendix A). In the limit of zero rotation λ equals $\ell(\ell + 1)$. We see that λ decreases towards the

centre of a star, indicating the increasing rotation velocity (refer also to Fig. 12 and the discussion later in the text).

3.2 Modelling

Our main aim was to find models that fit (within the observational errors) the value of the rotational frequency and the values of the highest amplitude modes from the sequence S_a.

We computed evolutionary and pulsational models for different parameters and searched for models that fit the value of f_1, a rotational frequency. The value of f_1 depends on both the surface rotational velocity (V_{surf}) and the stellar radius (R), both of which undergo changes along an evolutionary path. Consequently, within a reasonable range of initial parameters, it becomes possible to determine an evolution time at which the theoretical rotational frequency matches the observed value.

To establish a time measure, we selected effective temperature (T_{eff}). For intermediate and massive main sequence stars, T_{eff} exhibits a monotonically decreasing trend over time. Given that evolutionary models are provided for discrete time points, we applied Akima spline interpolation (Akima 1970) to pinpoint an accurate value of T_{eff} at which f_1 is accurately reproduced.

The pulsational frequencies of models that fit f_1 depend on model parameters like mass, initial rotational velocity, overshooting parameter, metallicity, etc. By fine-tuning the mass parameter, we identified models that also align with the frequency f_{13}, the dominant pulsational frequency. Initially, we utilized Akima spline interpolation to derive an approximate value for the mass (M). Subsequently, we increased the grid density around that point and repeated the interpolation for greater precision.

Subsequently, we sought models that also aligned with the frequency f_{11}. This was accomplished by adjusting the initial rotational velocity, $V_{surf,0}$. Once again, we employed interpolation to derive an approximate value for this parameter, followed by an increase in grid density around that point and repeating the interpolation process. As a result, our grid of models became non-uniform, with higher densities strategically placed where needed.

We iteratively applied this procedure to reproduce the frequencies f_{20} and f_{10}. Each iteration focused on determining one parameter to match a specific frequency. The frequency f_{20} was employed to derive the overshooting from the convective core, while f_{10} was utilized to fix the metallicity. Consequently, each model that successfully fits the rotational frequency f_1 and the pulsational frequencies f_{13}, f_{11}, f_{20}, f_{10} is characterized by specific values for T_{eff}, M, $V_{surf,0}$, f_{ov}, and Z.

From comparison of the observed and theoretical frequencies (Fig. 8), we concluded that other frequencies are also well reproduced by our models. The least satisfactory fits are observed for frequencies f_6, f_7, f_8, and f_{23}. The highest observed frequency from sequence S_a (f_{23}) is smaller than the theoretical counterpart. Interestingly, the frequency is reproduced by axisymmetric mode g_3. Therefore, the frequency may not be a part of a prograde sequence. Low frequencies f_6, f_7, f_8 exhibit larger dispersion from a regular structure than the theoretical counterparts.

We tested different input configurations. In our models, we assumed the initial hydrogen abundance $X = 0.7$ and used three different opacity data, i.e. OPAL, OP, and OPLIB.

All our models are given in Table 4 (models from 1 to 5). Models 1 to 3 were calculated with the OPLIB opacities. Model 4 was calculated with the OPAL data and Model 5 with the OP tables. In Model 2, no diffusion of the chemical elements was included. In all other models, chemical diffusion without radiative levitation was

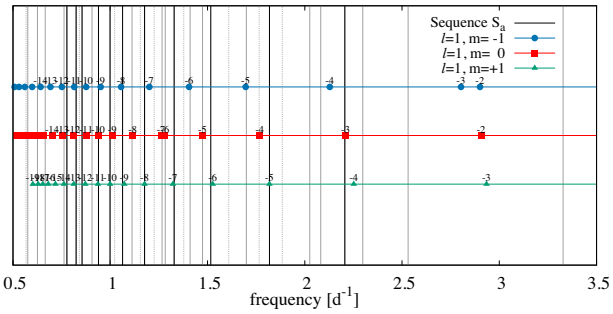

Figure 8. Comparison of the all observed oscillation spectrum with theoretical counterparts of dipole modes from Model 1. Solid vertical lines indicate independent frequencies while dotted lines represent combinations and harmonics. The left-hand axis has arbitrary units.

incorporated. In Model 3, we assumed that there was no rotational mixing of the chemical elements. All other models include mixing caused by different instabilities like Solberg-Hoiland Instability (SHI), the Secular Shear Instability (SSI), the Eddington–Sweet Circulation (ES), the Goldreisch-Schubert-Fricke Instability (GSF), and the Dynamical Shear Instability (DSI). A detailed description of the aforementioned instabilities can be found in Heger, Langer & Woosley (2000). In the calculations, we assumed a scaling factor of $f_c = 1/30$, describing the efficiency of rotationally induced instabilities to the diffusion coefficient (for more details, see Pinsonneault et al. 1989; Chaboyer & Zahn 1992; Heger, Langer & Woosley 2000) and a factor of $f_\mu = 0.05$, describing the sensitivity of the rotational mixing to the chemical element abundances gradient, ∇_μ (Heger, Langer & Woosley 2000).

The quality of the fit can be judged from Fig. 9, where we plotted the sequence S_a and theoretical counterparts of Models 1, 2, and 3. The observed period differences has a buoyancy glitches near a period of about 1.0–1.2 d. The models reproduce the overall shape of the period differences, but the glitches are not perfectly mapped in models. This may indicate that some layers with significant gradient of the chemical element abundances are missing in the models.

In Fig. 10, we presented the abundances of the CNO elements for Models 1, 2, and 3 near the core. Additionally, we plotted the Brunt–Väisälä frequency, N^2, for all models. In the case of Model 2 (calculated without an atomic diffusion), we observe a sharp change in the abundances of nitrogen (N) and oxygen (O), leading to small but distinct peaks in the Brunt–Väisälä frequency.

The position of the N^2 maximum varies among all models. It is deepest for Model 3 and shallowest for Model 1. However, this variation has a relatively minor impact on the frequencies corresponding to the S_a sequence.

As shown by Aerts et al. (2018) and Bowman & Michielsen (2021), the theoretical uncertainties dominate over observational uncertainties in the total error budget for model parameters. To account for the theoretical uncertainties, we considered five models with different theoretical input.

The uncertainties of model parameters arising from the observational uncertainties are connected with the frequency determination accuracy. To account for this effect, we performed a simulation, in which we randomized frequency values from Gaussian distributions instead of fitting the exact values of frequencies. We assumed that the mean values of the Gaussian distributions equal the frequencies and the standard deviations equal the frequency uncertainties. Therefore, the simulation effectively took into account frequencies within 3σ errors. In Fig. 6 on the HR diagram, we showed the effective

Table 4. Asteroseismic models of a Cen. The following columns include: model number (No.), uniform angular momentum transport coefficient ($D_{\rm uam}$), metallicity (Z), parameter of the exponential convective core overshooting ($f_{\rm ov}$), mass (M), surface rotational velocity ($V_{\rm surf}$), effective temperature ($\log T_{\rm eff}$), luminosity ($\log L/L_{\odot}$), radius (R), age from ZAMS (Age), hydrogen content of the convective core ($X_{\rm c}$), and mass of the convective core ($M_{\rm c}$). In the last column, we have given the value Π_0, defined in equation (2).

No.	$D_{\rm uam}$ $\times 10^5$ cm^2 s^{-1}	Z	$f_{\rm ov}$	M M$_\odot$	$V_{\rm surf}$ km s^{-1}	$\log T_{\rm eff}$	$\log L/L_{\odot}$	R $R_\odot$	age $\times 10^4$ yr	$X_{\rm c}$	$M_{\rm c}$ M$_\odot$	Π_0 s
					OPLIB, $X = 0.7$, rotational mixing							
1	20.37(12)	0.00954(16)	0.02674(32)	5.4501(67)	17.261(31)	4.2743(13)	3.0083(39)	3.0071(54)	2361(13)	0.58563(93)	1.3276(27)	11574.0(2.9)
					OPLIB, $X = 0.7$, rotational mixing, no diffusion							
2	18.9(2.6)	0.00952(20)	0.02667(37)	5.4518(72)	17.261(46)	4.2745(15)	3.0092(43)	3.0072(80)	2360(16)	0.58542(10)	1.3279(33)	11573.4(5.6)
					OPLIB, $X = 0.7$, no rotational mixing							
3	56.4(1.2)	0.01022(52)	0.02648(86)	5.443(28)	17.445(59)	4.2698(39)	2.999(13)	3.039(10)	2422(54)	0.5843(12)	1.3190(94)	11607.4(5.1)
					OPAL, $X = 0.7$, rotational mixing							
4	11.52(14)	0.01015(50)	0.02878(62)	5.443(26)	17.285(57)	4.2724(36)	3.002(12)	3.0113(99)	2287(50)	0.5925(11)	1.3291(91)	11591.8(2.6)
					OP, $X = 0.7$, rotational mixing							
5	20.906(60)	0.00827(11)	0.02516(44)	5.4848(45)	16.78(27)	4.28437(82)	3.0239(26)	2.9234(48)	2265(32)	0.58484(88)	1.3327(18)	11559.1(6.2)

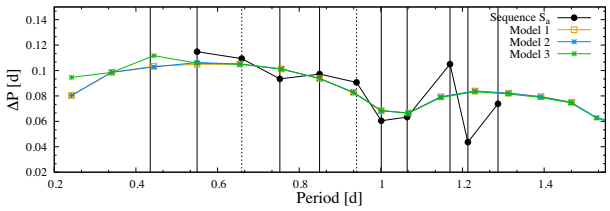

Figure 9. Comparison of period differences, ΔP between observations and theoretical counterparts of Models 1, 2, and 3.

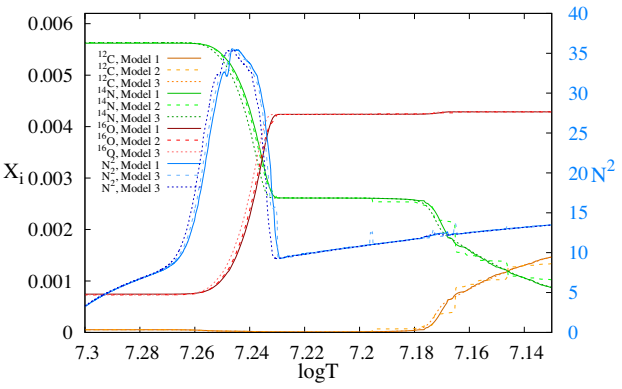

Figure 10. Left-hand axis: abundances of CNO elements for Models 1, 2, and 3. Right-hand axis: Brünt–Väisalä frequency, N^2.

temperatures and luminosities from the simulation connected with Model 1.

The distribution of some parameters from Model 1, which were constrained through our asteroseismic analysis, is shown in Fig. 11. We see that we manage to constrain precisely the mass, which is equal to $M = 5.4501(67)\,{\rm M}_\odot$. We derived also rather low metallicity, $Z = 0.00954(16)$. The rotational velocity equals to $17.261(31)\,{\rm km\,s^{-1}}$. The very important result is the constraint on the overshooting from the convective core. For a Cen, we derived quite efficient mixing of the layers adjacent to the convective core. The parameter of the exponentially decreasing overshooting (Herwig 2000) is equal to $f_{\rm ov} = 0.02674(32)$. The model parameters are rather strongly correlated, which can be seen in Fig. C1, where we showed two-dimensional distributions (so-called corner plot). Therefore, the uncertainties given in Table 4 have to be taken with caution, since these are simple standard deviations derived from distributions and they do not include correlations. The covariance matrices are given in Appendix C.

For Model 2, calculated without diffusion of elements, we derived slightly higher mass $M = 5.4518(72)\,{\rm M}_\odot$ and nearly the same metallicity $Z = 0.00952(20)$. The overshooting parameter and rotational velocity change very little in comparison with Model 1.

The results seem to be moderately sensitive to the rotational mixing processes. For Model 3, for which this mixing was suppressed, we derived a higher metallicity $Z = 0.01022(52)$ and smaller mass $M = 5.443(28)\,{\rm M}_\odot$ in comparison with Model 1. Though the values are within estimated uncertainties. The overshooting parameter and rotational velocity change very little.

Model 4, calculated with the OPAL opacity tables, closely resembles Model 1, although it exhibits a slightly higher metallicity $Z = 0.01022(52)$ and overshooting parameter $f_{\rm ov} = 0.02878(62)$. Model 4 is also marginally younger. More significant deviations are observed for Model 5, computed with the OP tables. This model features the lowest metallicity, $Z = 0.00827(11)$, and the

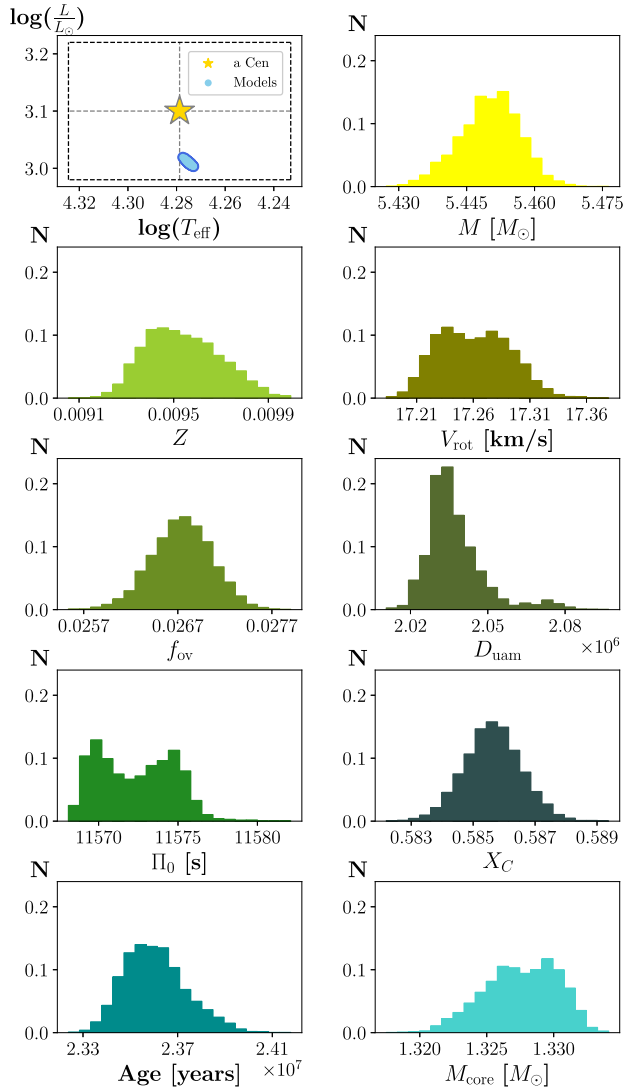

Figure 11. The models in the HR diagram and the distributions of parameters are: mass, metallicity, initial rotational velocity, overshooting parameter, and uniform angular momentum transport coefficient. *N* represents the relative number of models.

highest mass $M = 5.4848(45)\,\mathrm{M}_{\odot}$. Consequently, it is hotter and more luminous than all others. Nevertheless, the differences remain relatively modest.

The other very important constraint that was derived by means of our analysis is the co-called diffusion parameter of the uniform angular momentum transport, $D_{\rm uam}$. In MESA code, the transport of angular momentum is formulated as a diffusive process (e.g. Heger, Langer & Woosley 2000). The total diffusion coefficient is a sum of non-rotational and a rotational coefficients

$$D_{\rm tot} = D_{\rm rot} + D_{\rm non\text{-}rot}.$$

The rotational term consist itself from different factors

$$D_{\rm rot} = D_{\rm DSI} + D_{\rm SH} + D_{\rm SSI} + D_{\rm ES} + D_{\rm GSF},$$

where SHI, SSI, ES, GSF, and DSI are already mention rotational instabilities. The non-rotational part is equal to

$$D_{\rm non-rot} = D_{\rm uam} + D_{\rm conv} + D_{\rm sem},$$

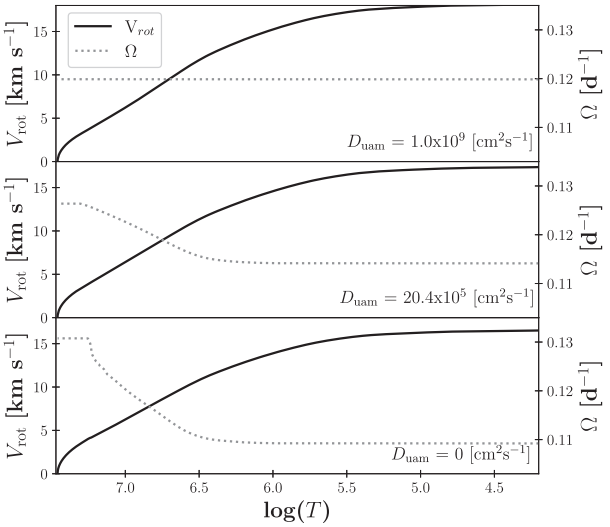

Figure 12. Rotation profiles for linear (left axis) and angular velocity (right axis) for three models with different values of the $D_{\rm uam}$. In the top panel, where $D_{\rm uam} = 1 \times 10^9$ cm^2 s^{-1}, there is a case of rigid rotation. In the bottom panel, with $D_{\rm uam} = 0$, there is a high gradient of rotational velocity. The middle panel, $D_{\rm uam} = 20.4 \times 10^5$ cm^2 s^{-1} represents the Model 1 (Table 4) of a Cen.

where $D_{\rm conv}$ and $D_{\rm sem}$ are diffusion coefficients for convection and semiconvection, respectively. $D_{\rm uam}$ is an artificial parameter that enforces constant angular momentum transport. The higher its value, the more uniform rotation we get. From tests, we deduced that for $D_{\rm uam} \sim 10^9$ cm^2 s^{-1}, we have a rigid rotation.

In order to get constraints on this parameter, we needed to assume one additional thing. Namely, four frequencies, which do not belong to sequences $S_{\rm a}, f_{12}, f_{14}, f_{15}$, and f_{18}, are $(\ell = 1, m = 0, g_8)$, $(\ell = 1, m = 0, g_7)$, $(\ell = 1, m = 0, g_6)$ and $(\ell = 1, m = 0, g_5)$ modes, respectively. This identification was made from a comparison of the observed spectrum of pulsational frequencies with theoretical counterparts for our asteroseismic models (see Fig. 8). We considered dipole modes with all possible azimuthal number. The aforementioned identification was the only one possible. Unfortunately, we cannot exclude higher mode degrees. Though dipole modes are the most probable due to the surface cancellation effect (see for example, Daszyńska-Daszkiewicz et al. 2002, 2015).

The differences between theoretical values of axisymmetric and prograde modes are highly sensitive to the rotational profile of the star. We successfully fitted four $m = 0$ frequencies, namely f_{12}, f_{14}, f_{15}, and f_{18}, by selecting an appropriate rotational profile. It became evident that the default values of the angular momentum transport coefficient in the MESA code are significantly too low to accommodate these four axisymmetric frequencies. A much more uniform rotation is required. Our asteroseismic models indicate a preference for $D_{\rm uam} = 20.37(12) \times 10^5$ cm^2 s^{-1}. A comparison of the rotational profiles calculated for different values of $D_{\rm uam}$ is presented in Fig. 12. The bottom panel illustrates the default rotational profiles from MESA, the upper panel displays the rigid rotation case, and the middle panel depicts the profile of our Model 1. The preferred rotation is nearly solid, suggesting the operation of an effective angular momentum transport mechanism within a Cen.

To evaluate the impact of frequency uncertainties on model parameters, we conducted an additional simulation, assuming a frequency accuracy of 0.001 d^{-1}. This is approximately an order of

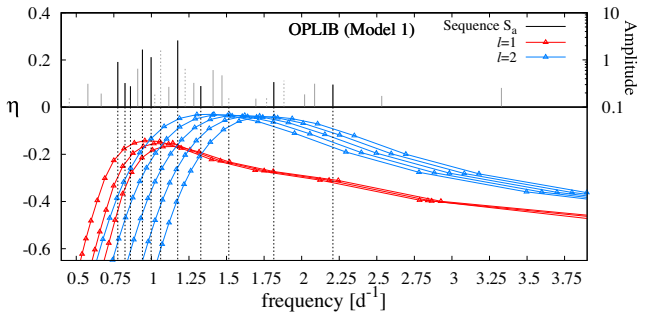

Figure 13. The instability parameter η for dipole and quadrupole modes for Model 1 (Table 4). We considered all possible azimuthal orders, m. The leftmost lines correspond to retrograde sectoral modes, the central lines represent axisymmetric modes, and the rightmost lines depict prograde sectoral modes.

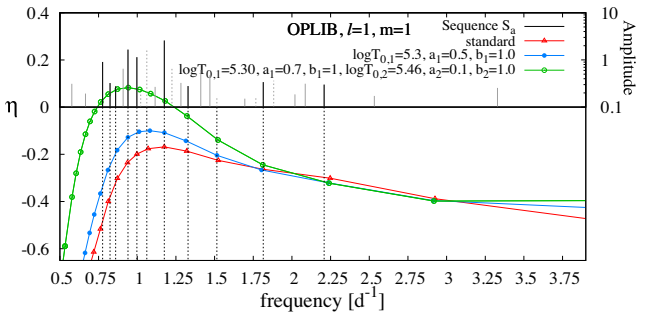

Figure 14. Instability parameter η for dipole prograde modes ($\ell = 1$, $m = 1$) for standard and modified opacity tables.

magnitude larger than the formal frequency errors. The simulation revealed an order of magnitude increase in uncertainties for $f_{\rm ov}$ and M. Other parameter uncertainties increased by a factor of 3 to 5. Despite the significant increase, the disparities between different models remained larger. This underscores that theoretical uncertainties exert a more substantial influence on derived parameters than the observational uncertainties.

3.3 Mode excitation

To examine the driving properties, we chose a representative models and calculated the non-adiabatic pulsations. As a measure of the driving or dumping of modes, we took the instability parameter, η (Stellingwerf 1978). This parameter is normalized to the range $\langle -1, +1\rangle$, where positive values indicate excited modes, and negative values indicate damped modes. The η parameter for dipole and quadrupole modes corresponding to Model 1 is plotted as a function of frequency in Fig. 13. We considered all possible azimuthal orders, $m = -1, 0, +1$ for $\ell = 1$ and $m = -2, -1, 0, +1, +2$ for $\ell = 2$.

As we can see, all considered theoretical modes are stable. The model cannot account for the excitation of the observed modes. This is partially due to the low metallicity of the Model 1, which is only about 0.0095. Similar situation occurs for other models calculated with the OPLIB and OPAL opacity tables. In general, the OPLIB opacities yield the highest instability parameter (Walczak et al. 2015), but the OPAL model (Model 4) has larger metallicity, which compensates the opacity table effect and results in a very similar values of the η parameter. The smaller value of of the instability parameter occur for the OP tables (Model 5).

Since the standard models cannot explain the presence of unstable modes, we decided to check the artificial increase of the opacity tables. Asteroseismic studies of B-type stars have shown that a significant increase in the opacity is needed to explain all observed frequencies (see e.g. Salmon et al. 2012; Daszyńska-Daszkiewicz et al. 2017; Szewczuk & Daszyńska-Daszkiewicz 2017, 2018; Walczak et al. 2019; Niemczura et al. 2022). We applied an opacity modification of the following form:

$$\kappa(T) = \kappa_0(T)\left[1 + \sum_{i=1}^{N} b_i \exp\left(-\frac{(\log T - \log T_{0,i})^2}{a_i^2}\right)\right],$$

where $\kappa_0(T)$ is the standard opacity profile, a_i and b_i are the width and height of the additional Gaussian bump, respectively, $T_{0,i}$ is its central temperature, and N is the number of added opacity bumps. We note that we choose the Model 1 as a reference model and we

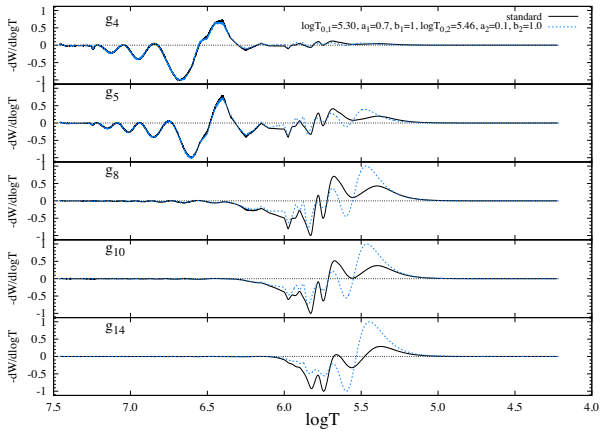

Figure 15. Differential work integral for five chosen modes of the standard and modified opacity model. See text for details.

did not change its parameters. We only modified opacity. Therefore, models with the changed opacity coefficient are not asteroseismic models of a Cen. Here, we wanted to show only the effect of the opacity increase.

The models with the modified opacity coefficient are shown in Fig. 14 in the η versus frequency plane. For clarity, we show only the dipole prograde modes ($\ell = 1$, $m = +1$). The standard model refers to unchanged OPLIB data, i.e. Model 1.

Increasing the opacity by 100 per cent ($b_1 = 1.0$, $a_1 = 0.5$) at $\log T_{0,1} = 5.3$, resulted in an increase in the instability parameter (violet line in Fig. 14), but the effect was unsatisfactory. The dipole modes still remained stable. We called this opacity change Modification 1.

We also examined the opacity increase at two temperatures, $\log T_{0,1} = 5.3$ and $\log T_{0,2} = 5.46$ (Modification 2). At both temperatures, we used $b_{1,2} = 1$ (100 per cent). For lower temperature, we assumed a wide bump, i.e. $a_1 = 0.7$. For higher temperature, we took $a_2 = 0.1$. This led to a substantial rise in the instability parameter (green line in Fig. 14. Nevertheless, the η for the highest frequencies was still negative.

In Fig. 15, we showed the differential work integral, $-{\rm d}W/{\rm d}\log T$, for five chosen dipole prograde modes, g_4, g_5, g_8, g_{10}, and g_{14}. The positive value of this quantity indicates regions inside of a star that drive pulsations. Negative values correspond to dumping regions. With a black solid line, we marked the standard opacity model (Model 1) and with a blue dotted line, we marked an opacity modified model corresponding to Modification 2.

From Fig. 15, we can notice that modes with radial orders from $n = 14$ to 8 are affected by our opacity changes. Near the $\log T \sim 5.5$, there is a significant increase of the driving of modes. On the other hand, modes with lower radial orders seem to be rather insensitive to such modification. The differential work integral of the mode g_4 merely changed. Therefore, some more sophisticated opacity table modifications are needed. However, the search for the most appropriate changes of the opacity coefficient is beyond the scope of this paper.

The studies of the increased opacity effect were inspired by the experimental work of Bailey et al. (2015), who found iron opacities much larger than predicted. An increase of the opacity was also found by Pradhan & Nahar (2018); Zhao et al. (2018); Nagayama et al. (2019); Hui-Bon-Hoa, Pain & Richard (2022). Both, experiments and asteroseismic modelling of B-type stars clearly indicate that something is missing in the currently available opacity tables.

4 CONCLUSIONS

An in-depth analysis of the time-resolved photometric data collected by *TESS* satellite has revealed that a Cen is a slowly pulsating B type star. The frequency spectrum consists of rotational frequency, its harmonics and numerous high order g-modes. We found a regular period spacing structure which, according to our analysis, is due to the presence of consecutive dipole prograde modes.

We managed to impose robust constraints on the stellar structure, particularly obtaining precise values for the overshooting parameter, $f_{\rm ov} \sim 0.027$. The metallicity and mass exhibit slight dependencies on the opacity tables. For the OPLIB and OPAL data, we derived $Z \sim 0.01$ and $M \sim 5.45\,{\rm M}_{\odot}$. The OP tables prefer lower metallicity of the order of 0.008 and a higher mass, $\sim 5.5\,{\rm M}_{\odot}$. Irrespective of the opacity tables used, the asteroseismic models consistently indicate a preference for rigid rotation.

All models listed in Table 4 reproduce precisely the rotational frequency, f_1 and pulsational frequencies from a series S_a: f_{10}, f_{11}, f_{13}, and f_{20}. The theoretical counterparts for other frequencies in the series exhibit slight deviations from the observed values. The largest difference, $0.05\ {\rm d}^{-1}$, occur for the frequency f_{23}.

Models 1, 2, and 4 accurately reproduce frequencies f_{12}, f_{14}, f_{15}, and f_{18} under the assumption that they are axisymmetric dipole modes. Models 3 (without rotational mixing) and 5 (with OP tables) cannot fit well with the f_{14} and f_{15} frequencies.

The frequencies f_{17} and f_{19} may correspond to dipole retrograde modes g_6 and g_5, respectively. These are well-reproduced by all models except for Model 3. The highest frequency, f_{27}, can be reproduced as $(\ell = 1, m = -1, {\rm g}_1)$ mode only in the case of Model 1.

The f_2 frequency may represent a dipole prograde mode, while the frequency f_3 could be either a dipole prograde or axisymmetric mode.

Frequencies that do not have counterparts among the dipole modes are f_4, f_9, f_{21}, f_{22}, f_{24}, f_{25}, and f_{26}. These frequencies might correspond to higher-degree modes.

The five distinct models outlined in Table 4 fit the frequencies from a series S_a equally well. Differences arise for other modes, but the absence of a definitive mode identification complicates the selection of the optimal model. Conversely, the variations in parameters among Models 1 to 5 are relatively minor. It appears that the parameters derived for a Cen are, to some extent, independent of uncertainties associated with the opacity table and incorporated physical processes such as rotational mixing and atomic diffusion.

The star a Cen is another main sequence star, for which, nearly solid body rotation is preferred. Other examples include the B-type stars HD 29589 (Niemczura et al. 2022), KIC 10526294 (Triana et al. 2015), and HD 201433 (Kallinger et al. 2017), A-type star KIC 11145123 (Kurtz et al. 2014), F-type stars KIC 9244992 (Saio et al. 2015), and KIC 7661054 (Murphy et al. 2016). Also, most of the detailed studied γ Doradus stars seem to be rigidly rotating (Van Reeth et al. 2018; Saio et al. 2021).

On the other hand, slightly steeper gradient of the rotation profile ient was found for B-type stars ν Eri, 12 Lac (Dziembowski & Pamyatnykh 2008), HD 129929 (Salmon et al. 2022), and HD 192575 (Burssens et al. 2023). Therefore, depending on the star, the internal rotation can be of different shape, and a lot of stars should be studied in order to formulate some more general conclusions.

Finally, the excitation of modes for standard opacity models is well below the expected level. Nearly all modes are stable from theoretical point of view. We have showed that significant opacity increase near the Z-bump is needed in order to get unstable modes.

Pulsations in chemically peculiar stars are considered rare occurrences; however, instances of such phenomena are documented. Notably, the extreme Helium stars V652 Her and BX Cir were recently identified as pulsating sources (Kilkenny, Worters & Baran 2024). The variability observed in these stars is likely induced by the κ mechanism, operating on the iron opacity peak at $\log T \sim 2 \times 10^5$ K (Saio 1993).

Research by Murphy et al. (2020a) demonstrated that the variability in many λ Boo stars is attributed to δ Sct pulsations. Additionally, a small percentage (approximately 4 per cent) of chemically peculiar Ap stars have been found to exhibit pulsations (Balona, Holdsworth & Cunha 2019; Cunha et al. 2019). A slightly larger fraction of pulsating Ap stars, nearly 6 per cent, was documented by Holdsworth et al. (2021, 2024). The chemical peculiarity of Ap stars is associated with a strong magnetic field, as highlighted by Saio (2005); the presence of a kG-strength magnetic field suppresses low-overtone p-modes. Conversely, high overtone p-modes could be excited by the κ-mechanism operating in the H ionization zone. This aligns with observations, as pulsating Ap stars typically lack evidence of low-overtone pulsations. An exception is KIC 11296437, which may be the first Ap star observed to pulsate simultaneously in high- and low-overtone modes (Murphy et al. 2020b).

Among B-type stars, Kochukhov et al. (2021) identified pulsations in eight out of 65 analysed mercury–manganese stars. Additionally, a few pulsating Ap- and Bp-type stars were discovered by Bowman et al. (2018).

The number of known pulsating chemically peculiar stars remains limited, with an even smaller subset examined asteroseismically (e.g. Shibahashi & Takata 1993; Briquet et al. 2012; Handler et al. 2012; Neiner et al. 2012; Pápics et al. 2012; Henrichs et al. 2013; Buysschaert et al. 2017, 2018). Consequently, any additional example is deemed highly significant in advancing our understanding of these phenomena.

ACKNOWLEDGEMENTS

This work was supported financially by the Polish National Science Centre grant 2018/29/B/ST9/01940. Calculations were carried out using resources provided by Wroclaw Centre for Networking and Supercomputing (http://wcss.pl), grant no. 265.

This work has made use of data from the European Space Agency (ESA) mission *Gaia* (https://www.cosmos.esa.int/gaia), processed by the *Gaia* Data Processing and Analysis Consortium (DPAC; https://www.cosmos.esa.int/web/gaia/dpac/consortium). Funding for the DPAC has been provided by national institutions, in particular the institutions participating in the *Gaia* Multilateral Agreement.

This paper includes data collected by the *TESS* mission. Funding for the *TESS* mission is provided by the NASA Explorer Program.

This research made use of LIGHTKURVE, a PYTHON package for Kepler and TESS data analysis.

Some of the data presented in this paper were obtained from the Mikulski Archive for Space Telescopes (MAST) at the Space Telescope Science Institute. The specific observations analyzed can be accessed via https://doi.org/10.17909/t9-nmc8-f686 and via https://doi.org/10.17909/0cp4-2j79 is operated by the Association of Universities for Research in Astronomy, Inc., under NASA contract NAS5–26555. Support to MAST for these data is provided by the NASA Office of Space Science via grant NAG5–7584 and by other grants and contracts.

The authors are indebted to Wojciech Szewczuk for fruitful discussions on the subject of this article.

DATA AVAILABILITY

The data underlying this article may be shared by the corresponding author upon reasonable request.

REFERENCES

Aerts C., 2021, Rev. Mod. Phys., 93, 015001
Aerts C., Christensen-Dalsgaard J., Kurtz D. W., 2010, Asteroseismology. Springer Science+Business Media, Netherlands
Aerts C. et al., 2018, ApJS, 237, 15
Aerts C., Mathis S., Rogers T. M., 2019, ARA&A, 57, 35
Akima H., 1970, J. ACM, 17, 589
Alastuey A., Jancovici B., 1978, ApJ, 226, 1034
Asplund M., Grevesse N., Sauval A. J., Scott P., 2009, ARAA, 47, 481
Astropy Collaboration, 2022, ApJ, 935, 167
Bailey J. E. et al., 2015, Nature, 517, 56
Ballot J., Lignières F., Reese D. R., 2013, in Goupil M., Belkacem K., Neiner C., Lignières F., Green J. J., eds, Lecture Notes in Physics, Vol. 865. Springer-Verlag, Berlin, p. 91
Balona L. A., Holdsworth D. L., Cunha M. S., 2019, MNRAS, 487, 2117
Baran A. S., Koen C., 2021, AcA, 71, 113
Bildsten L., Ushomirsky G., Cutler C., 1996, ApJ, 460, 827
Bohlender D. A., Rice J. B., Hechler P., 2010, A&A, 520, A44
Bouabid M. P., Dupret M. A., Salmon S., Montalbán J., Miglio A., Noels A., 2013, MNRAS, 429, 2500
Bowman D. M., 2020, Front. Astron. Space Sci., 7, 70
Bowman D. M., Michielsen M., 2021, A&A, 656, A158
Bowman D. M., Buysschaert B., Neiner C., Pápics P. I., Oksala M. E., Aerts C., 2018, A&A, 616, A77
Briquet M. et al., 2012, MNRAS, 427, 483
Burssens S. et al., 2023, Nat. Astron., 7, 913
Buysschaert B., Neiner C., Briquet M., Aerts C., 2017, A&A, 605, A104
Buysschaert B. et al., 2018, A&A, 616, A148
Chaboyer B., Zahn J. P., 1992, A&A, 253, 173
Chapman S., Lindzen R., 1970, Atmospheric tides. Thermal and gravitational. Dordrecht, Reidel
Christophe S., Ballot J., Ouazzani R. M., Antoci V., Salmon S. J. A. J., 2018, A&A, 618, A47
Colgan J., Kilcrease D. P., Magee N. H., Abdallah J., Sherrill M. E., Fontes C. J., Hakel P., Zhang H. L., 2015, High Energ. Dens. Phys., 14, 33
Colgan J. et al., 2016, ApJ, 817, 116
Cunha M. S. et al., 2019, MNRAS, 487, 3523
Cyburt R. H. et al., 2010, ApJS, 189, 240
Daszyńska-Daszkiewicz J., Dziembowski W. A., Pamyatnykh A. A., Goupil M.-J., 2002, A&A, 392, 151
Daszyńska-Daszkiewicz J., Dziembowski W. A., Pamyatnykh A. A., 2003, A&A, 407, 999
Daszyńska-Daszkiewicz J., Dziembowski W. A., Pamyatnykh A. A., 2005, A&A, 441, 641
Daszynska-Daszkiewicz J., Dziembowski W. A., Pamyatnykh A. A., 2007, AcA, 57, 11
Daszyńska-Daszkiewicz J., Dziembowski W. A., Jerzykiewicz M., Handler G., 2015, MNRAS, 446, 1438
Daszyńska-Daszkiewicz J., Pamyatnykh A. A., Walczak P., Colgan J., Fontes C.J., Kilcrease D.P., 2017, MNRAS, 466, 2284
Degroote P. et al., 2010, Nature, 464, 259
Dewitt H. E., Graboske H. C., Cooper M. S., 1973, ApJ, 181, 439
Dziembowski W. A., 1971, AcA, 21, 289
Dziembowski W. A., 1977, AcA, 27, 203
Dziembowski W. A., Pamyatnykh A. A., 2008, MNRAS, 385, 2061
Dziembowski W. A., Moskalik P., Pamyatnykh A. A., 1993, MNRAS, 265, 588
Dziembowski W. A., Daszyńska-Daszkiewicz J., Pamyatnykh A. A., 2007, MNRAS, 374, 248
Endal A. S., Sofia S., 1978, ApJ, 220, 279
Ferguson J. W., Alexander D. R., Allard F., Barman T., Bodnarik J. G., Hauschildt P. H., Heffner-Wong A., Tamanai A., 2005, ApJ, 623, 585
Fitzpatrick E. L., 2004, in Witt A. N., Clayton G. C., Draine B. T., eds, ASP Conf. Ser. Vol. 309, Astrophysics of Dust. Astron. Soc. Pac., San Francisco, p. 33
Fossati L. et al., 2015, A&A, 582, A45
Fuller G. M., Fowler W. A., Newman M. J., 1985, ApJ, 293, 1
Gaia Collaboration, 2018, A&A, 616, A1
Gaia Collaboration, 2023, A&A, 674, A1
Garcia S., Van Reeth T., De Ridder J., Tkachenko A., IJspeert L., Aerts C., 2022, A&A, 662, A82
Gautschy A., Saio H., 1993, MNRAS, 262, 213
Ginsburg A. et al., 2019, AJ, 157, 98
Głębocki R., Gnaciński P., 2005, in Favata F., Hussain G. A. J., Battrick B., eds, ESA Special Publication Vol. 560, 13th Cambridge Workshop on Cool Stars, Stellar Systems and the Sun. p. ESA Publication Division 571
Gontcharov G. A., Mosenkov A. V., 2017, MNRAS, 472, 3805
Handler G. et al., 2012, MNRAS, 424, 2380
Heger A., Langer N., Woosley S. E., 2000, ApJ, 528, 368
Henrichs H. F. et al., 2013, A&A, 555, A46
Herwig F., 2000, A&A, 360, 952
Holdsworth D. L. et al., 2021, MNRAS, 506, 1073
Holdsworth D. L. et al., 2024, MNRAS, 527, 9548
Hui-Bon-Hoa A., Pain J. C., Richard O., 2022, A&A, 658, A70
Iglesias C. A., Rogers F. J., 1996, ApJ, 464, 943
Itoh N., Totsuji H., Ichimaru S., Dewitt H. E., 1979, ApJ, 234, 1079
Itoh N., Hayashi H., Nishikawa A., Kohyama Y., 1996, ApJS, 102, 411
Jenkins J. M. et al., 2016, in Chiozzi G., Guzman J. C., eds, SPIE Conf. Ser. Vol. 9913, Software and Cyberinfrastructure for Astronomy IV, 99133E
Kallinger T. et al., 2017, A&A, 603, A13
Kilkenny D., Worters H. L., Baran A. S., 2024, MNRAS, 527, 8402
Kochukhov O., Khalack V., Kobzar O., Neiner C., Paunzen E., Labadie-Bartz J., David-Uraz A., 2021, MNRAS, 506, 5328
Krtička J., Mikulášek Z., Prvák M., Niemczura E., Leone F., Wade G., 2020, MNRAS, 493, 2140
Kurtz D. W., Saio H., Takata M., Shibahashi H., Murphy S. J., Sekii T., 2014, MNRAS, 444, 102
Langanke K., Martínez-Pinedo G., 2000, Nucl. Phys. A, 673, 481
Lee U., Saio H., 1997, ApJ, 491, 839
Leroy B., 2012, A&A, 545, A50
Lightkurve Collaboration, 2018, Lightkurve: Kepler and TESS time series analysis in Python, Astrophysics Source Code Library. preprint (ascl:1812.013)
Lomb N. R., 1976, Ap&SS, 39, 447
Miglio A., Montalbán J., Noels A., Eggenberger P., 2008, MNRAS, 386, 1487
Mombarg J. S. G., Dotter A., Rieutord M., Michielsen M., Van Reeth T., Aerts C., 2022, ApJ, 925, 154
Moravveji E., Aerts C., Pápics P. I., Triana S. A., Vandoren B., 2015, A&A, 580, A27
Moravveji E., Townsend R. H. D., Aerts C., Mathis S., 2016, ApJ, 823, 130

Murphy S. J., Fossati L., Bedding T. R., Saio H., Kurtz D. W., Grassitelli L., Wang E. S., 2016, MNRAS, 459, 1201
Murphy S. J., Paunzen E., Bedding T. R., Walczak P., Huber D., 2020a, MNRAS, 495, 1888
Murphy S. J., Saio H., Takada-Hidai M., Kurtz D. W., Shibahashi H., Takata M., Hey D. R., 2020b, MNRAS, 498, 4272
Nagayama T. et al., 2019, Phys. Rev. Lett., 122, 235001
Neiner C., Alecian E., Briquet M., Floquet M., Frémat Y., Martayan C., Thizy O., MIMES Collaboration, 2012, A&A, 537, A148
Niemczura E., Walczak P., Mikołajczyk P., Schöller M., Hummel C. A., Hubrig S., Różański T., 2022, MNRAS, 514, 5640
Oda T., Hino M., Muto K., Takahara M., Sato K., 1994, At. Data Nucl. Data Tables, 56, 231
Pápics P. I. et al., 2012, A&A, 542, A55
Pápics P. I., Moravveji E., Aerts C., Tkachenko A., Triana S. A., Bloemen S., Southworth J., 2014, A&A, 570, A8
Pápics P. I., Tkachenko A., Aerts C., Van Reeth T., De Smedt K., Hillen M., Østensen R., Moravveji E., 2015, ApJ, 803, L25
Pápics P. I. et al., 2017, A&A, 598, A74
Paxton B., Bildsten L., Dotter A., Herwig F., Lesaffre P., Timmes F., 2011, ApJS, 192, 3
Paxton B. et al., 2013, ApJS, 208, 4
Paxton B. et al., 2015, ApJS, 220, 15
Paxton B. et al., 2018, ApJS, 234, 34
Paxton B. et al., 2019, ApJS, 243, 10
Pedersen M. G., Escorza A., Pápics P. I., Aerts C., 2020, MNRAS, 495, 2738
Pedersen M. G. et al., 2021, Nat. Astron., 5, 715
Pinsonneault M. H., Kawaler S. D., Sofia S., Demarque P., 1989, ApJ, 338, 424
Pols O. R., Tout C. A., Eggleton P. P., Han Z., 1995, MNRAS, 274, 964
Potekhin A. Y., Chabrier G., 2010, Contrib. Plasma Phys., 50, 82
Pradhan A. K., Nahar S. N., 2018, in Workshop on Astrophysical Opacities. p. 79, preprint (arXiv:1801.02085)
Ricker G., 2019, in AAS/Division for Extreme Solar Systems Abstracts. p. 100.01
Ricker G. R. et al., 2015, J. Astron. Telesc. Instrum. Syst., 1, 014003
Rogers F. J., Nayfonov A., 2002, ApJ, 576, 1064
Saio H., 1993, MNRAS, 260, 465
Saio H., 2005, MNRAS, 360, 1022
Saio H., Kurtz D. W., Takata M., Shibahashi H., Murphy S. J., Sekii T., Bedding T. R., 2015, MNRAS, 447, 3264
Saio H., Takata M., Lee U., Li G., Van Reeth T., 2021, MNRAS, 502, 5856
Salmon S., Montalbán J., Morel T., Miglio A., Dupret M. A., Noels A., 2012, MNRAS, 422, 3460
Salmon S. J. A. J., Moyano F. D., Eggenberger P., Haemmerlé L., Buldgen G., 2022, A&A, 664, L1
Salpeter E. E., 1954, Aust. J. Phys., 7, 373
Saumon D., Chabrier G., van Horn H. M., 1995, ApJS, 99, 713
Scargle J. D., 1982, ApJ, 263, 835
Seaton M. J., 2005, MNRAS, 362, L1
Sharma A. N., Bedding T. R., Saio H., White T. R., 2022, MNRAS, 515, 828
Shibahashi H., 1979, PASJ, 31, 87
Shibahashi H., Takata M., 1993, PASJ, 45, 617
Shultz M. E. et al., 2022, MNRAS, 513, 1429
Stellingwerf R. F., 1978, AJ, 83, 1184
Szewczuk W., Daszyńska-Daszkiewicz J., 2017, MNRAS, 469, 13
Szewczuk W., Daszyńska-Daszkiewicz J., 2018, MNRAS, 478, 2243
Szewczuk W., Daszyńska-Daszkiewicz J., Walczak P., 2017, in European Physical Journal Web of Conferences. p. 03012, preprint (arXiv:1701.01256)
Szewczuk W., Walczak P., Daszyńska-Daszkiewicz J., 2021, MNRAS, 503, 5894
Szewczuk W., Walczak P., Daszyńska-Daszkiewicz J., Moździerski D., 2022, MNRAS, 511, 1529
Takata M., Ouazzani R. M., Saio H., Christophe S., Ballot J., Antoci V., Salmon S. J. A. J., Hijikawa K., 2020, A&A, 635, A106
Tassoul M., 1980, ApJS, 43, 469
Timmes F. X., Swesty F. D., 2000, ApJS, 126, 501
Townsend R. H. D., 2003a, MNRAS, 340, 1020
Townsend R. H. D., 2003b, MNRAS, 343, 125
Townsend R. H. D., 2020, MNRAS, 497, 2670
Townsend R. H. D., Teitler S. A., 2013, MNRAS, 435, 3406
Triana S. A., Moravveji E., Pápics P. I., Aerts C., Kawaler S. D., Christensen-Dalsgaard J., 2015, ApJ, 810, 16
Unno W., Osaki Y., Ando H., Saio H., Shibahashi H., 1989b, Nonradial oscillations of stars. Tokyo, Japan, University of Tokyo Press
Van Reeth T. et al., 2018, A&A, 618, A24
Waelkens C., 1991, A&A, 246, 453
Walczak P., Fontes C. J., Colgan J., Kilcrease D. P., Guzik J. A., 2015, A&A, 580, L9
Walczak P. et al., 2019, MNRAS, 485, 3544
Zhang C. et al., 2018, ApJ, 854, 168
Zhao L., Eissner W., Nahar S. N., Pradhan A. K., 2018, in ASP Conf. Ser. Vol. 515, Workshop on Astrophysical Opacities. Astron. Soc. Pac., San Francisco, p. 89
Zima W., 2006, A&A, 455, 227
Zima W. et al., 2006, A&A, 455, 235

APPENDIX A: LAPLACE TIDAL EQUATIONS

Within the framework of traditional approximation of rotation the displacement of the mass element in the co-rotating frame, $\boldsymbol{\xi} = (\xi_r, \xi_\theta, \xi_\phi)$, for mode with an azimuthal order m is expressed as

$$\xi_{\rm r} = \tilde{\xi}_{\rm r}(r)\Theta(\theta)\mathrm{e}^{\mathrm{i}(\mathrm{m}\varphi-\sigma_{\rm c}\mathrm{t})} \tag{A1}$$

$$\xi_\theta = \frac{\tilde{\xi}_{\rm h}(r)}{\sin\theta}\hat{\Theta}(\theta)\,\mathrm{e}^{i(m\varphi-\sigma_{\rm c}t)} \tag{A2}$$

$$\xi_\phi = \frac{\tilde{\xi}_{\rm h}(r)}{i\sin\theta}\tilde{\Theta}(\theta)\,\mathrm{e}^{i(m\varphi-\sigma_{\rm c}t)}, \tag{A3}$$

where, $\tilde{\xi}_{\rm r}$ and $\tilde{\xi}_h$ are radial and horizontal displacement amplitude that are found by solving the oscillation equations (Bildsten, Ushomirsky & Cutler 1996; Lee & Saio 1997; Townsend 2003a, 2020, Appendix B). In the adopted convention, prograde modes have a positive value of the azimuthal order, i.e. $m > 0$. $\sigma_{\rm c} = \sigma - m\Omega$ is the pulsational frequency in the co-rotating reference frame, Ω is the rotation angular velocity and σ is the oscillation frequency in the inertial reference frame. In general, $\sigma_{\rm c}$ and Ω are functions of the radius, r. The Hough functions, Θ, $\hat{\Theta}$, and $\tilde{\Theta}$, are obtained by solving Laplace tidal equations

$$\left[(1-\mu^2)\frac{\mathrm{d}}{\mathrm{d}\mu} + ms\mu\right]\Theta = (s^2\mu^2-1)\hat{\Theta}, \tag{A4}$$

$$\left[(1-\mu^2)\frac{\mathrm{d}}{\mathrm{d}\mu} - ms\mu\right]\hat{\Theta} = \left[\lambda(1-\mu^2)-m^2\right]\Theta, \tag{A5}$$

$$\tilde{\Theta} = m\Theta - s\mu\hat{\Theta}. \tag{A6}$$

Here, $\mu = \cos\theta$, s is the spin parameter defined as $s \equiv 2\Omega/\sigma_{\rm c}$, λ is an eigenvalue, which is used in pulsational equations (see Appendix B).

APPENDIX B: PULSATIONAL EQUATIONS WITH TRADITIONAL APPROXIMATION OF ROTATION

The differential equations of stellar oscillations in the framework of traditional approximation are solved using the so-called Magnus Multiple Shooting scheme. The method is described in details in an excellent paper by Townsend & Teitler (2013). We have modified

the method by introducing the dynamical grid density. The density is now increased whenever it is needed.

The equations that are solved are presented below. We basically follow the Dziembowski formulation (Dziembowski 1971) with modification by Unno et al. (1989). The variables are written in dimensionless form

$$y_1 = \frac{\tilde{\xi}_r}{r}, \tag{B1}$$

$$y_2 = \frac{1}{gr}\left(\frac{\tilde{p}}{\rho} + \tilde{\Phi}\right), \tag{B2}$$

$$y_3 = \frac{1}{gr}\left(\tilde{\Phi}\right), \tag{B3}$$

$$y_4 = \frac{1}{g}\left(\frac{\mathrm{d}\tilde{\Phi}}{\mathrm{d}r}\right), \tag{B4}$$

$$y_5 = \frac{\delta S}{c_P}, \tag{B5}$$

$$y_6 = \frac{\delta L_R}{L_R}. \tag{B6}$$

Within traditional approximation the mode degree, ℓ, that occurs in the standard pulsational equations, has to be replaced by an effective harmonic degree, ℓ_e, defined as

$$\ell_e = \frac{\sqrt{1+4\lambda}-1}{2}, \tag{B7}$$

where λ is an eigenvalue of Laplace tidal equations. Variables $\tilde{p}$, $\tilde{\Phi}$, S, and L_R are amplitudes of pressure, gravitational potential, entropy, and radiative luminosity perturbations. c_P is specific heat at constant pressure, g is gravitational acceleration, and ρ is density.

In the limit of zero rotation, ℓ_e defined by equation B7 tends to the standard meaning, i.e. the total number of node planes and the Hough functions tends to spherical harmonic.

With the definitions given by equations B1–B7, the pulsational equations are as follow

$$\frac{\mathrm{d}y_1}{\mathrm{d}\ln r} = (V_g - 3)y_1 + \left[\frac{\ell_e(\ell_e+1)}{c_1\omega^2} - V_g\right]y_2 + V_g y_3 + v_T y_5, \tag{B8}$$

$$\frac{\mathrm{d}y_2}{\mathrm{d}\ln r} = \left(c_1\omega^2 - A\right)y_1 + (A - U + 1)y_2 - Ay_3 + v_T y_5, \tag{B9}$$

$$\frac{\mathrm{d}y_3}{\mathrm{d}\ln r} = (1-U)y_3 + + y_4, \tag{B10}$$

$$\frac{\mathrm{d}y_4}{\mathrm{d}\ln r} = UAy_1 + UV_g y_2 + [\ell_e(\ell_e+1) - UV_g]y_3 - Uy_4 - Uv_T y_5, \tag{B11}$$

$$\begin{aligned}\frac{\mathrm{d}y_5}{\mathrm{d}\ln r} &= V\left[\nabla_{ad}(U - c_1\omega^2) - 4(\nabla_{ad} - \nabla) + c_2\right]y_1 \\ &+ V\left[\frac{\ell_e(\ell_e+1)}{c_1\omega^2}(\nabla_{ad} - \nabla) - c_2\right]y_2 \\ &+ Vc_2 y_3 + V\nabla_{ad} y_4 + V\nabla(4 - \kappa_S)y_5 - V\nabla y_6, \\ \frac{\mathrm{d}y_6}{\mathrm{d}\ln r} &= \left[\ell_e(\ell_e+1)\frac{\nabla_{ad} - \nabla}{\nabla} - \varepsilon_{ad}c_3 V\right]y_1 \\ &+ \left[\varepsilon_{ad}c_3 V - \ell_e(\ell_e+1)\left(\frac{\nabla_{ad}}{\nabla} + \frac{c_3}{c_1\omega^2}\right)\right]y_2 \\ &+ \left[\ell_e(\ell_e+1)\frac{\nabla ad}{\nabla} - \varepsilon_{ad}c_3 V\right]y_3 \\ &+ \left[c_3\varepsilon_S - \frac{\ell_e(\ell_e+1)}{V\nabla} - \mathrm{i}\omega c_4\right]y_5 - \frac{\mathrm{d}\ln L_R}{\mathrm{d}\ln r}y_6,\end{aligned}$$

where $\omega = (\sigma - m\Omega)\sqrt{\frac{R^3}{GM}}$ is the dimensionless pulsational frequency and

$$A = \frac{r}{g}N^2, \tag{B12}$$

$$V_g = \frac{V}{\Gamma_1} = -\frac{1}{\Gamma_1}\frac{\mathrm{d}\ln p}{\mathrm{d}\ln r}, \tag{B13}$$

$$U = \frac{\mathrm{d}\ln M_r}{\mathrm{d}\ln r} = \frac{4\pi\rho r^3}{M_r}, \tag{B14}$$

$$c_1 = \frac{r^3}{R^3}\frac{M}{M_r}, \tag{B15}$$

$$c_2 = (\kappa_{ad} - 4\nabla_{ad})V\nabla + \nabla_{ad}\left(\frac{\mathrm{d}\ln\nabla_{ad}}{\mathrm{d}\ln r} + V\right), \tag{B16}$$

$$c_3 = \frac{4\pi r^3\rho\varepsilon_N}{L_R}, \tag{B17}$$

$$c_4 = \frac{4\pi r^3\rho T c_P}{L_R}\sqrt{\frac{GM}{R^3}}. \tag{B18}$$

$$\kappa_T = \left(\frac{\partial\ln\kappa}{\partial\ln T}\right)_\rho, \quad \kappa_\rho = \left(\frac{\partial\ln\kappa}{\partial\ln\rho}\right)_T, \tag{B19}$$

$$\kappa_{ad} = \left(\frac{\partial\ln\kappa}{\partial\ln p}\right)_S = \kappa_T\nabla_{ad} + \frac{\kappa_\rho}{\Gamma_1}, \kappa_S = c_P\left(\frac{\partial\ln\kappa}{\partial S}\right)_P = \kappa_T - v_T\kappa_\rho, \tag{B20}$$

$$\varepsilon_T = \left(\frac{\partial\ln\varepsilon_N}{\partial\ln T}\right)_\rho, \quad \varepsilon_T = \left(\frac{\partial\ln\varepsilon_N}{\partial\ln\rho}\right)_T, \tag{B21}$$

$$\varepsilon_{ad} = \left(\frac{\partial\ln\varepsilon_N}{\partial\ln T}\right)_S = \varepsilon_T\nabla_{ad} + \frac{\varepsilon_\rho}{\Gamma_1}, \tag{B22}$$

$$\varepsilon_S = \left(\frac{\partial\ln\varepsilon_N}{\partial S}\right)_P = \varepsilon_T - v_T\varepsilon_\rho, \tag{B23}$$

$$v_T = -\left(\frac{\partial\ln\rho}{\partial\ln T}\right)_P, \quad \Gamma_1 = \left(\frac{\partial\ln P}{\partial\ln\rho}\right)_{ad}. \tag{B24}$$

R and M are the radius and mass of the star, respectively, ε_N is the energy generated in nuclear reactions, κ is the opacity coefficient, M_r is the mass enclosed by a sphere of a radius r and G is the gravitational constant.

Differential equations need boundary conditions. There are three conditions in the star centre, where $r = 0$

$$y_1 c_1\omega^2 = \ell_e y_2, \tag{B25}$$

$$y_4 = \ell_e y_3, \tag{B26}$$

$$y_5 = 0. \tag{B27}$$

Other three conditions are given at the star surface ($r = R$)

$$y_1\left\{1 + \frac{\left[\frac{\ell_e(\ell_e+1)}{\omega^2} - 4 - \omega^2\right]}{V}\right\} - y_2 + y_3\left\{1 + \frac{\left[\frac{\ell_e(\ell_e+1)}{\omega^2} - \ell_e - 1\right]}{V}\right\} = 0, \tag{B28}$$

$$(\ell_e+1)y_3 + y_4 = 0, \tag{B29}$$

$$(2 - 4\nabla_{ad}V)y_1 + 4\nabla_{ad}V(y_2 - y_3) + 4y_5 - y_6 = 0. \tag{B30}$$

The amplitude of the horizontal displacement is equal to

$$\tilde{\xi}_h = \frac{1}{(\sigma - \Omega)^2 r}\left(\frac{\tilde{p}}{\rho} + \tilde{\Phi}\right) = \frac{gy_2}{\omega^2}, \tag{B31}$$

APPENDIX C: CORRELATIONS OF MODEL PARAMETERS

Most of parameter derived in our analysis show strong correlations. This is evident in Fig. C1, where we presented a corner plot depicting the relationships among mass, metallicity, initial rotational velocity, overshooting parameter, uniform angular momentum transport coefficient, and effective temperature for Model 1. Models 2–5 are depicted in Fig. C2

The covariance matrices for $D_{\rm uam}$, Z, $f_{\rm ov}$, M, $V_{\rm surf}$, and $\log T_{\rm eff}$ of Models 1–5 are given below

Model 1

$$\begin{pmatrix} 1.3\times10^{8} & -5.4\times10^{-1} & 2.1\times10^{-1} & 1.8\times10^{1} & -1.2\times10^{2} & 4.3 \\ -5.4\times10^{-1} & 2.4\times10^{-8} & 1.6\times10^{-8} & -9.8\times10^{-7} & 4.0\times10^{-6} & -2.0\times10^{-7} \\ 2.1\times10^{-1} & 1.6\times10^{-8} & 1.0\times10^{-7} & -1.3\times10^{-6} & -2.7\times10^{-6} & -1.3\times10^{-7} \\ 1.8\times10^{1} & -9.8\times10^{-7} & -1.3\times10^{-6} & 4.4\times10^{-5} & -1.3\times10^{-4} & 7.9\times10^{-6} \\ -1.2\times10^{2} & 4.0\times10^{-6} & -2.7\times10^{-6} & -1.3\times10^{-4} & 9.7\times10^{-4} & -3.2\times10^{-5} \\ 4.3 & -2.0\times10^{-7} & -1.3\times10^{-7} & 7.9\times10^{-6} & -3.2\times10^{-5} & 1.6\times10^{-6} \end{pmatrix}$$

Model 2

$$\begin{pmatrix} 6.7\times10^{10} & -3.9\times10^{1} & 5.0\times10^{1} & 6.3\times10^{2} & -1.1\times10^{4} & 2.9\times10^{2} \\ -3.9\times10^{1} & 3.8\times10^{-8} & 5.0\times10^{-9} & -1.2\times10^{-6} & 7.8\times10^{-6} & -3.0\times10^{-7} \\ 5.0\times10^{1} & 5.0\times10^{-9} & 1.4\times10^{-7} & -1.5\times10^{-6} & -7.1\times10^{-6} & -5.7\times10^{-8} \\ 6.3\times10^{2} & -1.2\times10^{-6} & -1.5\times10^{-6} & 5.1\times10^{-5} & -1.7\times10^{-4} & 9.6\times10^{-6} \\ -1.1\times10^{4} & 7.8\times10^{-6} & -7.1\times10^{-6} & -1.7\times10^{-4} & 2.1\times10^{-3} & -6.0\times10^{-5} \\ 2.9\times10^{2} & -3.0\times10^{-7} & -5.7\times10^{-8} & 9.6\times10^{-6} & -6.0\times10^{-5} & 2.3\times10^{-6} \end{pmatrix}$$

Model 3

$$\begin{pmatrix} 1.3\times10^{10} & -4.8\times10^{1} & -6.1\times10^{1} & 2.5\times10^{3} & -5.9\times10^{3} & 3.6\times10^{2} \\ -4.8\times10^{1} & 2.6\times10^{-7} & 3.8\times10^{-7} & -1.4\times10^{-5} & 2.85\times10^{-5} & -1.9\times10^{-6} \\ -6.1\times10^{1} & 3.8\times10^{-7} & 7.2\times10^{-7} & -2.2\times10^{-5} & 3.7\times10^{-5} & -2.9\times10^{-6} \\ 2.5\times10^{3} & -1.4\times10^{-5} & -2.2\times10^{-5} & 7.7\times10^{-4} & -1.5\times10^{-3} & 1.1\times10^{-4} \\ -5.9\times10^{3} & 2.8\times10^{-5} & 3.7\times10^{-5} & -1.5\times10^{-3} & 3.3\times10^{-3} & -2.1\times10^{-4} \\ 3.6\times10^{2} & -1.9\times10^{-6} & -2.9\times10^{-6} & 1.1\times10^{-4} & -2.1\times10^{-4} & 1.5\times10^{-5} \end{pmatrix}$$

Model 4

$$\begin{pmatrix} 1.7\times10^{8} & -2.4 & -3.8 & 1.4\times10^{2} & -2.9\times10^{2} & 1.9\times10^{1} \\ -2.4 & 2.5\times10^{-7} & 2.7\times10^{-7} & -1.3\times10^{-5} & 2.7\times10^{-5} & -1.8\times10^{-6} \\ -3.8 & 2.7\times10^{-7} & 3.8\times10^{-7} & -1.5\times10^{-5} & 2.6\times10^{-5} & -2.0\times10^{-6} \\ 1.4\times10^{2} & -1.3\times10^{-5} & -1.5\times10^{-5} & 6.6\times10^{-4} & -1.4\times10^{-3} & 9.2\times10^{-5} \\ -2.9\times10^{2} & 2.75\times10^{-5} & 2.6\times10^{-5} & -1.4\times10^{-3} & 3.2\times10^{-3} & -2.0\times10^{-4} \\ 1.9\times10^{1} & -1.8\times10^{-6} & -2.0\times10^{-6} & 9.2\times10^{-5} & -2.0\times10^{-4} & 1.3\times10^{-5} \end{pmatrix}$$

Model 5

$$\begin{pmatrix} 3.4\times10^{7} & 0.6 & -0.2 & -1.2\times10^{1} & 8.3\times10^{1} & -4.2 \\ 0.6 & 1.3\times10^{-8} & -1.5\times10^{-8} & -1.2\times10^{-7} & 2.3\times10^{-6} & -9.1\times10^{-8} \\ -0.2 & -1.5\times10^{-8} & 2.0\times10^{-7} & -1.7\times10^{-6} & -1.0\times10^{-5} & 7.2\times10^{-8} \\ -1.0\times10^{1} & -1.2\times10^{-7} & -1.7\times10^{-6} & 2.0\times10^{-5} & 5.6\times10^{-5} & 1.3\times10^{-6} \\ 8.3\times10^{1} & 2.3\times10^{-6} & -1.0\times10^{-5} & 5.6\times10^{-5} & 7.5\times10^{-4} & -1.5\times10^{-5} \\ -4.3 & -9.1\times10^{-8} & 7.2\times10^{-8} & 1.3\times10^{-6} & -1.5\times10^{e-5} & 6.7\times10^{-7} \end{pmatrix}$$

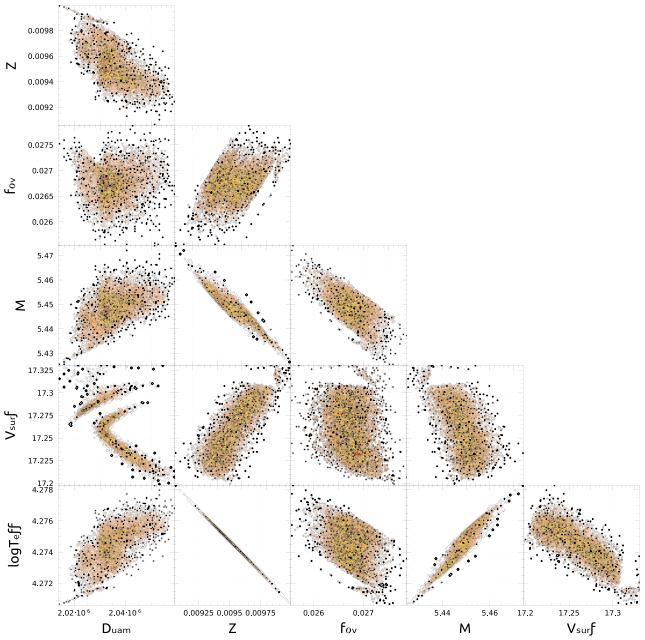

Figure C1. Two-dimensional distributions showing mutual correlations between models parameters for Model 1.

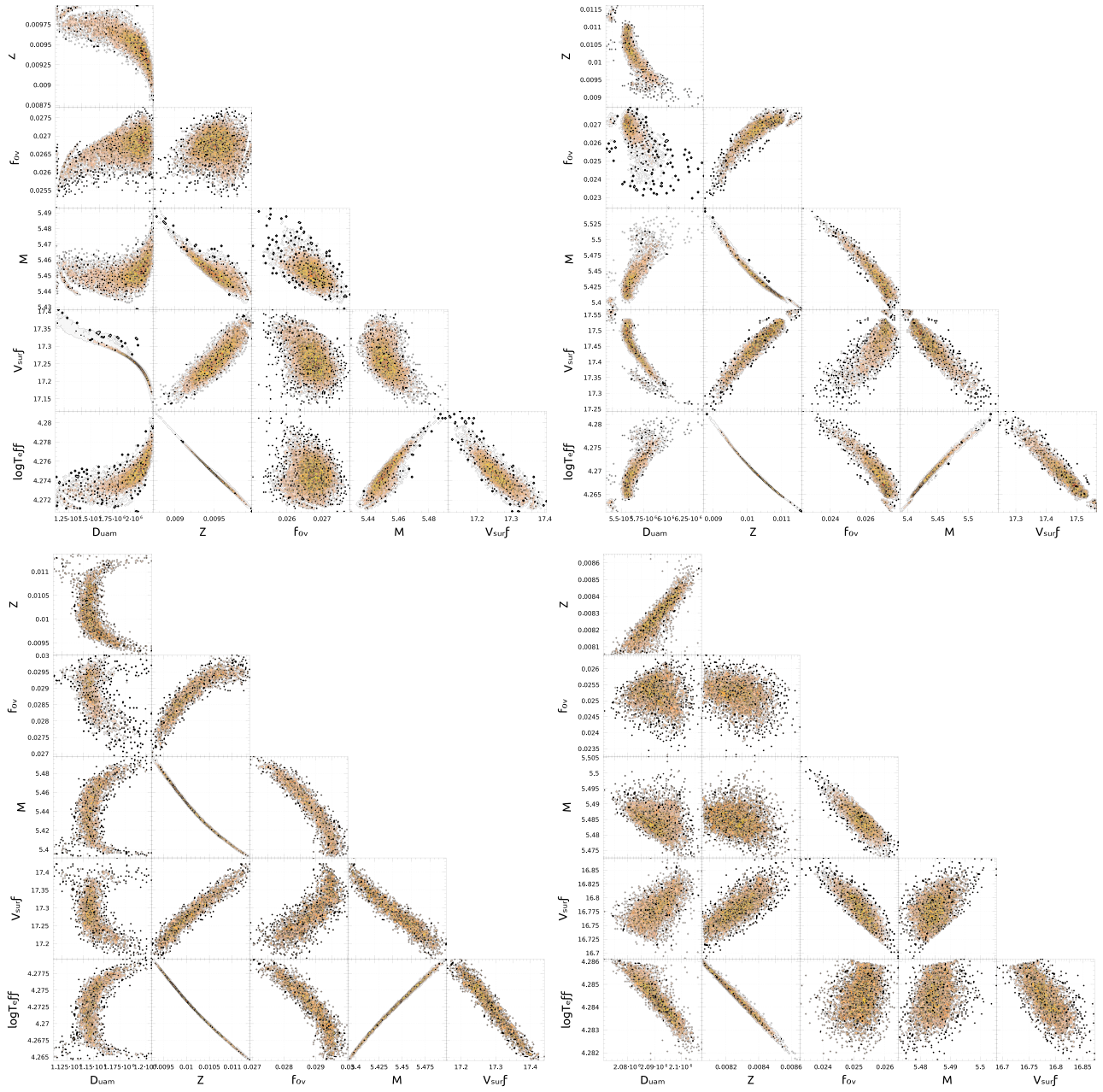

Figure C2. The same as in fig. C1 but for Model 2 (upper left), Model 2 (upper right), Model 4 (bottom left), and Model 5 (bottom right).

This paper has been typeset from a TEX/LATEX file prepared by the author.